UNIVERSITÄT OSNABRÜCK

Preparation of $SrTiO_3$ (001) Surfaces Studied by SPA-LEED

Master's thesis submitted as a part of the examination for the degree

of

Master of Science in Physics

Author: Nandhini RAVINDRAN

Matriculation number: 988301

First examiner: Prof. Dr. Joachim WOLLSCHLÄGER

Second examiner: Dr. Karsten KÜPPER

Osnabrück, 23. February 2023

Table of contents

1 Introduction

To make life easier in this fast paced world, cutting edge research and new technology have immense contribution to make. Taking the control of a surface means understanding the nook and corner of its physical and chemical properties by acknowledging and appreciating its wondrous applications in strengthening the manufacturing sector. One of the notable applications is fabrication of high quality devices [1]. Spintronics is important in contributing to the advancements in the field of storage density and memory. Spintronics outperforms conventional electronics by having the spin to process and store information. One of the breakthroughs in this field is the giant magnetoresistance effect (GMR) by Albert Fert and Peter Grünberg in 1988 [2]. It is based on spin-dependent transport and this effect is applied in hard disks. The first 16 gigabyte disk drive based on GMR was made by IBM in the year 1997 [3]. Tunnelling magnetoresistance (TMR) is another spintronic device that is very similar to GMR which was discovered by M. Julliére in 1975 [4]. TMR effect happens in magnetic tunnelling junctions (MTJs). A TMR device consists of two ferromagnetic layers that are separated by an ultra thin insulating material (less than about 2 nm) [5]. Spin-dependent quantum mechanical tunnelling of electrons happens between the ferromagnets leading to a change in electrical resistance. High degree of spin-polarisation at Fermi level is required to build high performance magnetoresistive devices. However, it was found that the performance of devices were not any better despite having epitaxial oxide metal junctions with good spin-polarisation. It was suspected that surface modifications at the interface could be a reason [6, 7]. Hence, a substrate like STO with robust spin-polarisation supports the oxide films and paves way for the development of functional materials like TMR structures in the field of spintronics [8].

The research for this master thesis was carried out to study and analyse the effect of different cleaning conditions on the substrate, Strontium Titanate ($SrTiO_3$), abbreviated as STO. It has high breakdown strength and hence used in the application of high voltage capacitor [9]. The cost efficient cubic perovskite $SrTiO_3$ has an excellent thermal and mechanical stability [10] which is applied in SOFC (Solid oxide fuel cell design). The temperature dependent dielectric property of STO substrate paves way for designing tunable terahertz devices [11].

A surface sensitive technique called spot profile analysis on low energy diffraction was the key for the analysis done in this work. SPA-LEED is a high resolution spot profile analysing technology

that gives information about the surface morphology, such as steps, terrace widths, roughness or any surface defects.

In chapter 2, the basic theoretical background required to understand this thesis is explained followed by chapter 3, where the information of material used for the study is explained. Chapter 4 deals with the experimental set-up. Chapter 5 presents the measured data with its appropriate evaluation and discussion. Chapter 6 summarises the research work and concludes with an outlook for further research of this topic.

2 Theory

This chapter is a gateway to understand the basics of crystallography. An insight into the three and two dimensional crystal structures is elucidated. Diffraction on periodic structures is discussed followed by the key focus of this master thesis, the theory of spot profile analysis on low energy electron diffraction.

2.1 Bulk lattices

In solid state physics, the periodic arrangement of atoms or group of atoms is defined as a crystal. It contains a three dimensional lattice. Each point of the lattice contains a basis. The basis of the lattice is the set of fundamental vectors $\vec{a}, \vec{b}, \vec{c}$ presented together with the unit cell (Fig 2.1). There are multiple possibilities to choose the size and shape of a unit cell as it depends only on the translational symmetry $(\vec{R})$. The smallest periodically repeated spatial structure in the lattice is called a primitive unit cell [12].
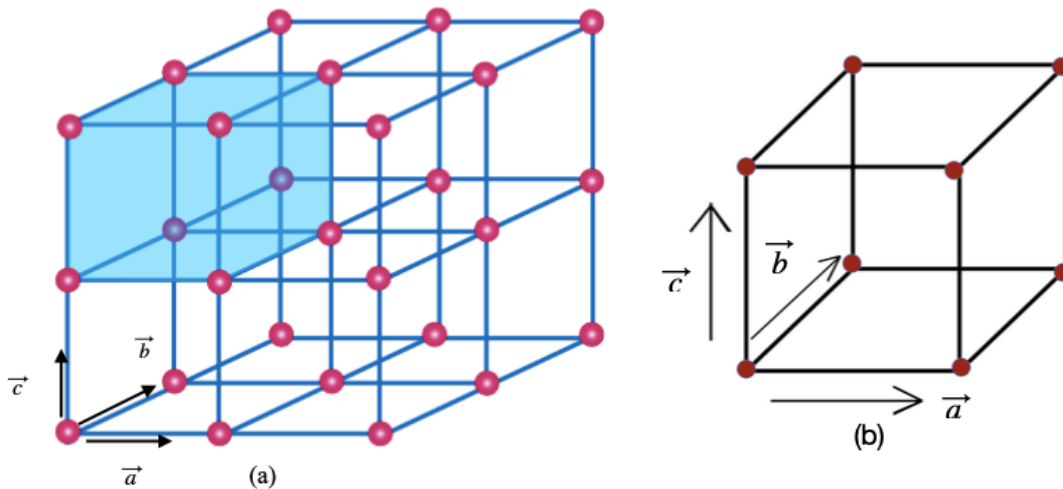
Fig 2.1: (a) Crystal structure with lattice vectors $\vec{a}, \vec{b}, \vec{c}$ (b) A single unit cell

The fundamental lattice vectors $\vec{a}, \vec{b}, \vec{c}$ describe the entire translational symmetry $(\vec{R})$ of the bulk crystal as defined by,

$$\vec{R} = n_1 \vec{a} + n_2 \vec{b} + n_3 \vec{c}, \text{ with } n_i \in \mathbb{Z}$$ (2.1)

Every bulk crystal is a periodic arrangement of unit cells represented by one of the Bravais lattices. There are fourteen Bravais lattices in three dimensional crystal.
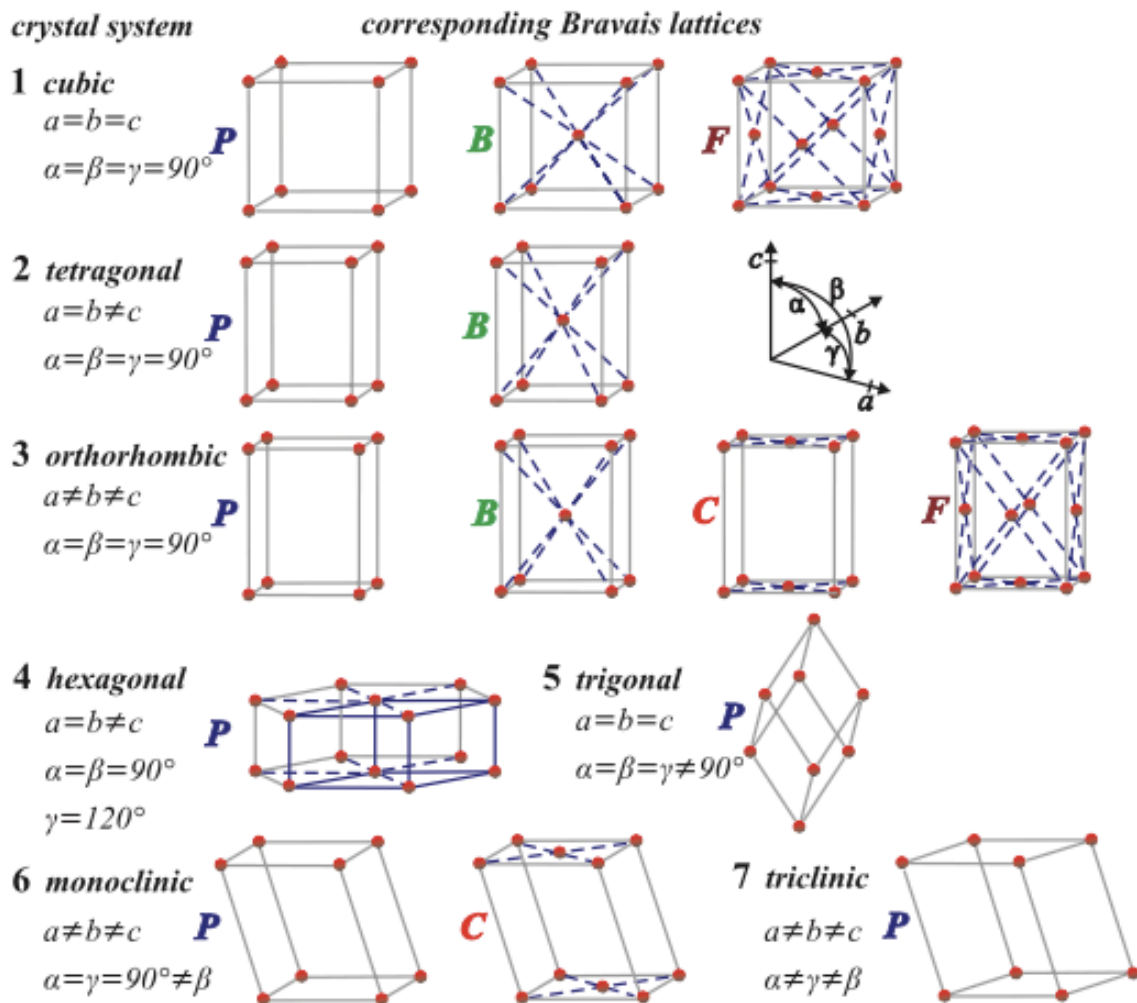

Fig 2.2: Schematic representation of 14 Bravais lattices of three dimensional crystals. Here the letters P,B,F and C denote primitive, body-centered, face-centered and base-centered unit cells [12]

Crystal lattices could be classified based on additional symmetries apart from translational symmetry mentioned earlier. Based on the different symmetry operations, crystal lattices are classified into seven different crystal systems. They are cubic, tetragonal, orthorhombic, trigonal, monoclinic and triclinic as seen in (Fig 2.2). These crystal systems are differentiable in correspondence to the magnitude of fundamental lattice vectors $\vec{a}, \vec{b}, \vec{c}$ and their angles α, β, γ. For example, a cubic crystal has $|\vec{a}| = |\vec{b}| = |\vec{c}|$ and $\alpha = \beta = \gamma = 90°$ [12]. STO is a cubic perovskite structure. The sublattices of Sr and Ti are simple cubic while oxygen forms an fcc sublattice (Fig 3.1).

5

Miller indices (h, k, l) are three numbers that characterise the crystal lattice planes. The intersection points of the crystal lattice plane with three crystal axis x, y and z is used to calculate the Miller indices. (Fig 2.3) shows different set of Miller indices.
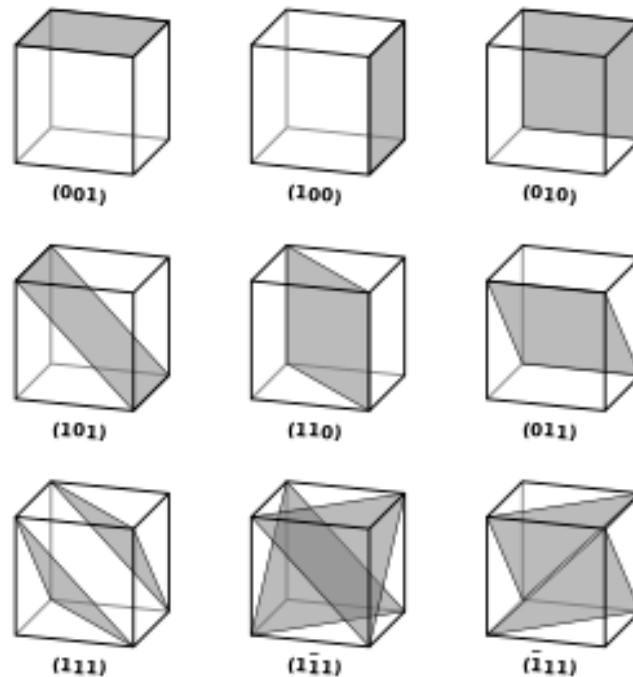

Fig 2.3: The diagram shows examples of different set of Miller indices. The grey part is the representation of planes.

The notation of negative numbers is given with an over score. Miller indices for planes could be explained with (Fig 2.4), here the plane intersects the x axis at point 'a'. It runs parallel along y and z axes. (a, ∞, ∞) are the intersections of the plane with the axis, as seen in (Fig 2.4). Since Miller indices are the reciprocals of the parameters of each crystal face, henceforth (a/a, a/∞, a/∞) is (100). Similarly, it applies to other sides of the planes.

The different use of representing Miller indices according to its purpose is given below,

• [h k l] represents a direction
• <h k l> represents a family of directions
• (h k l) represents a plane
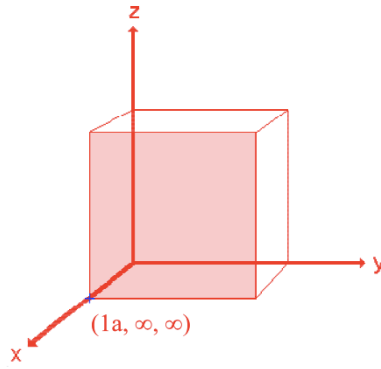• {h k l} represents a family of planes

Fig 2.4: An example of Miller indices are (1,0,0) for the plane (100) intersecting at point 'a'.

2.1.1 Reciprocal lattice and diffraction in 3D structures

The concept of reciprocal lattice is vital as it is the tool for interpretation of diffraction patterns. Hence, it is used in the study of bulk or surface analysing techniques like X-ray diffraction (XRD) and low energy electron diffraction (LEED).

For every crystal lattice in real space, a reciprocal lattice can be defined. It is given by fundamental reciprocal lattice vectors $\vec{a}*, \vec{b}*, \vec{c}*$:

$$\vec{a}* = 2\pi \frac{\vec{b} \times \vec{c}}{\vec{a} \cdot (\vec{b} \times \vec{c})} \ , \ \vec{b}* = 2\pi \frac{\vec{c} \times \vec{a}}{\vec{a} \cdot (\vec{b} \times \vec{c})} \ , \ \vec{c}* = 2\pi \frac{\vec{a} \times \vec{b}}{\vec{a} \cdot (\vec{b} \times \vec{c})} \qquad (2.2)$$

The volume of the unit cell is $\vec{a} \cdot (\vec{b} \times \vec{c})$. The fundamental reciprocal lattice vectors are directly linked to crystallographic fundamental lattice vectors $\vec{a}, \vec{b}, \vec{c}$. The set of all reciprocal lattice points can be expressed by the reciprocal lattice vector,

$$\vec{G}_{hkl} = h\vec{a}* + k\vec{b}* + l\vec{c}* \ \text{ with } \ h, k, l \in \mathbb{Z} . \qquad (2.3)$$

Vectors in the direct lattice have the dimensions of [length]; vectors in the reciprocal lattice have the dimensions of [l/length] [13].

The phenomenon of scattering is the redirection of light when an electromagnetic wave interacts with an obstacle. Diffraction is the elastic scattering of electromagnetic waves at long range ordered periodic structures like crystals [12].

7

In elastic scattering, the scattered light has the same frequency as the incident wave. The waves scattered at different parallel lattice planes interfere with each other resulting in intense peaks at certain scattering angles, known as Bragg reflections as shown in (Fig 2.5).
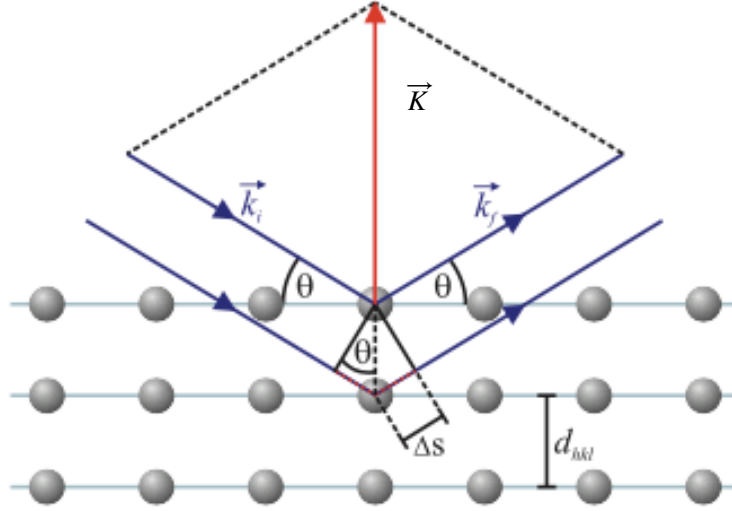

Fig 2.5: An illustration of Bragg's law which shows the incoming wave vector $\vec{k}_i$ getting scattered with a scattering angle θ at different lattice planes with a layer distance of d_{hkl} and the reflected waves with wave vector $\vec{k}_f$ reflected at adjacent lattice planes exhibit a path difference $2\Delta S$. The scattering wave vector K is perpendicular to the plane and is given as $\vec{K} = \vec{k}_f - \vec{k}_i$ [12].

In 1913, W. L Bragg and W. H. Bragg explained Bragg reflections as an incident wave vector $\vec{k}_i$ with a wavelength λ hitting a crystal at an angle θ with respect to lattice planes {hkl}. The incident wave is reflected at different parallel lattice planes at an angle θ. The reflected waves with wave vector $\vec{k}_f$ reflected at adjacent lattice planes exhibit a path difference $2\Delta S$. The difference between final and incident wave vector gives the scattering wave vector $\vec{K}$, which is given as,

$$\vec{K} = \vec{k}_f - \vec{k}_i \qquad (2.4)$$

The Bragg condition is fulfilled and the constructive interference occurs when the path difference between the reflected waves is a multiple of their wavelength. Thus the Bragg condition [14] is given as,

$$2d_{hkl} sin\theta = n\lambda , \ n \in \mathbb{N} \qquad (2.5)$$

where, d_{hkl} is the distance between the hkl-lattice planes, θ the angle of incidence and reflection, n the order of the Bragg reflection and λ the wavelength of the incident beam.

In 1912, Max von Laue presented three Laue conditions, which is an alternative diffraction condition [15]. They are given as,

$$\vec{K} \cdot \vec{a} = 2\pi h, \ \vec{K} \cdot \vec{b} = 2\pi k, \ \vec{K} \cdot \vec{c} = 2\pi l \ \text{with} \ h, k, l \in \mathbb{Z} \tag{2.6}$$

where $\vec{K}$ is the scattering vector, $\vec{a}, \vec{b}, \vec{c}$ are the basis vectors of the crystal lattice and h, k, l are the integer numbers corresponding to the Miller indices for constructive interference of waves reflected (or scattered) at the set of lattice planes (hkl). This could be applied to reciprocal space with reciprocal lattice vectors $\vec{a}*, \vec{b}*, \vec{c}*$. Thus, the Laue condition is fulfilled when each scattering vector $\vec{K}$ coincides with a reciprocal lattice point. This results in constructive interference and the reciprocal lattice vectors can be considered as the Bragg peak positions. Hence, the relation is given as,

$$\vec{K} = \vec{G}_{hkl} = h\vec{a}* + k\vec{b}* + l\vec{c}* \tag{2.7}$$

Thus, (Eqn. 2.7) gives the Laue equation, where the scattering vector $\vec{K}$ is equal to the reciprocal lattice vector $\vec{G}_{hkl}$.

2.2 Surface lattices

The topmost atomic layers in a crystal are called a surface. The crystal surface is described by a two dimensional lattice. The 2D lattice is given as,

$$\vec{R} = n_1\vec{a} + n_2\vec{b} \tag{2.8}$$

Surface effects lead to reconstruction and relaxation of the surface lattice. Reconstruction might also happen due to the adsorption of foreign atoms on the surface. These reconstructions are called superstructures.

There are five Bravais lattices and 17 plane groups that classify the two-dimensional crystal structures [16]. The five types of two-dimensional Bravais lattices are stated below and shown in (Fig 2.6)

- oblique lattice $|a| \neq |b|, \gamma \neq 90°$,

- rectangular lattice $|a| \neq |b|, \gamma = 90°$,

- centered rectangular lattice $|a| = |b|, \gamma \neq 90°$

- square lattice $|a| = |b|, \gamma = 90°$,
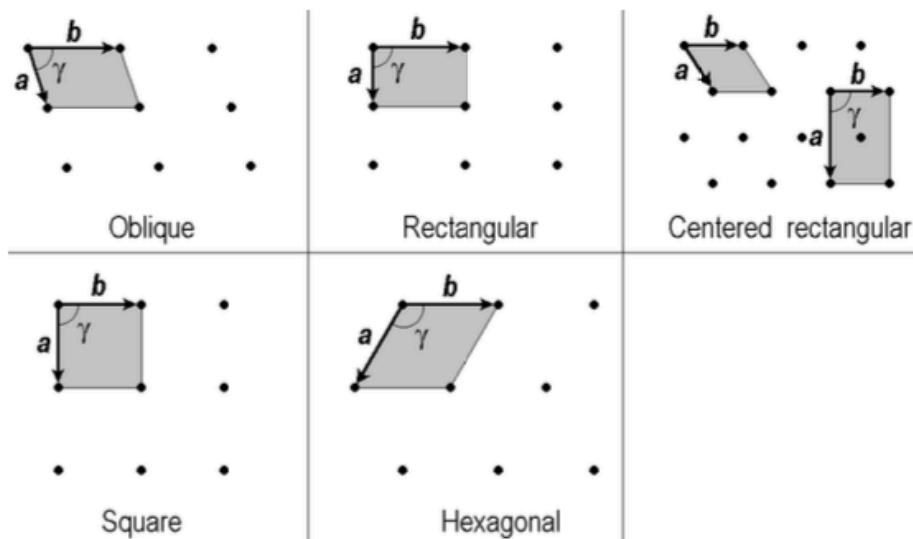
- hexagonal lattice $|a| = |b|, \gamma = 120°$.

Fig 2.6: Schematic representation of the five two-dimensional Bravais lattices. The vectors $\vec{a}$ and $\vec{b}$ represent the unit cell [17].

2.2.1 Reciprocal lattice and diffraction in 2D structures

The reduced dimension of a two-dimensional structure is due to the of lack of periodicity in vertical direction. A reciprocal lattice for an ideal three-dimensional crystal has Bragg points and for a two-dimensional crystal, it has Bragg rods (Fig 2.7). These Bragg rods in 2D are due to the reduced translational symmetry along the vertical direction [17].
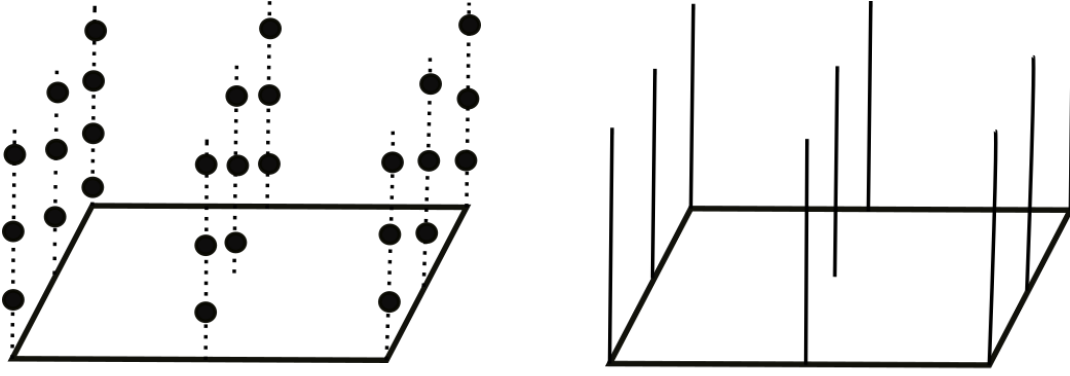
Fig 2.7: Illustration of reciprocal lattices for an ideal three-dimensional crystal (left) with Bragg points. Here, dotted lines are drawn to guide the eyes. Two-dimensional crystal (right) with Bragg rods

That is, in real space, the periodicity along the surface normal can be assumed to be infinite which means that in the reciprocal space, the diffraction reflexes are extremely close to each other resulting in rod shaped Bragg peaks [18].

Hence, the study of surfaces in two-dimensional structure is given by the reciprocal lattice as,

$$\vec{G}_{hk} = h\vec{a}* + k\vec{b}* \ \text{ with } \ h, k \in \mathbb{Z} \tag{2.9}$$

and the reciprocal vectors with $\vec{n}$, the unit perpendicular to the surface, is given as,

$$\vec{a}* = 2\pi \frac{\vec{b} \times \vec{n}}{\vec{a} \cdot (\vec{b} \times \vec{n})} \ , \ \vec{b}* = 2\pi \frac{\vec{n} \times \vec{a}}{\vec{a} \cdot (\vec{b} \times \vec{n})} \tag{2.10}$$

In two dimensional space, the Laue condition is given as,

$$\vec{K}_{\parallel} = \vec{k}_{f\parallel} - \vec{k}_{i\parallel} = \vec{G}_{hk} \tag{2.11}$$

with

$$\vec{G}_{hk} = h\vec{a}* + k\vec{b}* \tag{2.12}$$

where only the components of wave actors parallel to the surface are relevant, since the diffraction along the perpendicular components $\vec{K}_{\perp}$ are satisfied.

2.3 Low-energy electron diffraction

Electron diffraction is a breakthrough in the field of surface science. It is a product of Davisson and Germer's invention at Bell Laboratories in 1927 [19]. Low-energy electron diffraction is a technique used to determine the surface structure of crystalline samples. Electrons with an energy of 20-500 eV [20] are elastically backscattered with an incident normal to the sample surface. The de Broglie wavelength of electrons used for LEED is given as [21],

$$\lambda_e = \frac{h}{\sqrt{2m_e E_{kin}}} \tag{2.13}$$

where, h and m_e are the Planck's constant and the electron mass, respectively. E_{kin} is the kinetic energy of the electrons. The technique is surface sensitive and only electrons backscattered in the near-surface region can interfere. Thus, the (periodic) surface structure can be studied by LEED. In order to evaluate information from the diffraction pattern, the concept of reciprocal space is used [22]. Since only the surface is probed, Bragg rods form in reciprocal space (Fig 2.7). To study the diffraction pattern an Ewald sphere is constructed. The electrons are incident normal to a surface with wave vector $\vec{k}_i$. The backscattered wave vectors are denoted as $\vec{k}_f$ and they terminate on intersection with the Bragg rods (Fig 2.8).
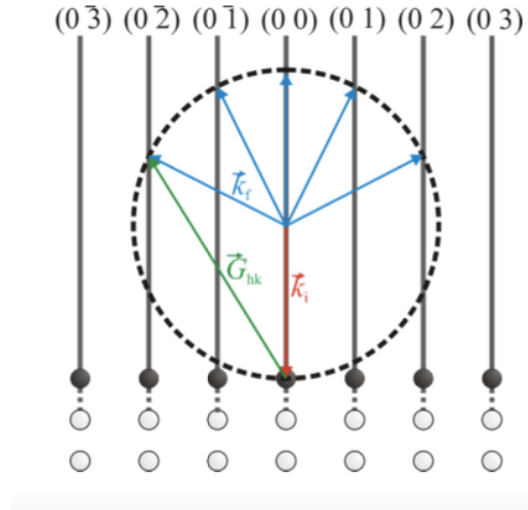

Fig 2.8: Illustration of Ewald construction. This figure shows the construction of diffraction pattern. $\vec{k}_i$ is the initial set of electrons hitting the surface normally at (00) lattice rod. Constructive diffraction is given if the Bragg rod intersects the Ewald sphere [23]. The backscattered wave vectors are denoted as $\vec{k}_f$. The scattering wave vector $\vec{G}_{hk}$ is given by its parallel component $\vec{K}_{\parallel}$ (Eqn. 2.11).

The radius of Ewald sphere could be defined by the magnitude $|k_i| = |k_f|$. The two-dimensional Laue condition is fulfilled when $\vec{k}_f$ terminates on the intersection of Ewald sphere and Bragg rod, resulting in diffraction. There is a fixed angle of electron beam incidence on the surface in LEED experiments. Hence, the radius of the Ewald sphere could be modified by changing the kinetic energy of the electrons [12]. Expansion of the Ewald sphere leads to smaller diffraction angles and more diffraction spots.

LEED is a highly surface sensitive method. Therefore, the slightest of deviations on the ideal surface reflects on the diffraction pattern. Periodic changes like reconstruction or terraces for vicinal surfaces may cause additional diffraction spots and lead to a change in intensity distribution while local point defects show only diffuse background intensity [24]. Hence, the analysis of spot intensities and widths provide qualitative and quantitative information on the density of defects.

2.3.1 Kinematic diffraction theory

There are two different types of theories for diffraction. Kinematic theory neglects multiple scattering. Multiple scattering is where a beam scattered gets scattered again and again by scatterers located at other positions. Dynamic diffraction theory is for multiple scattering of electrons at the crystal but includes heavy calculations when describing surface with defects.
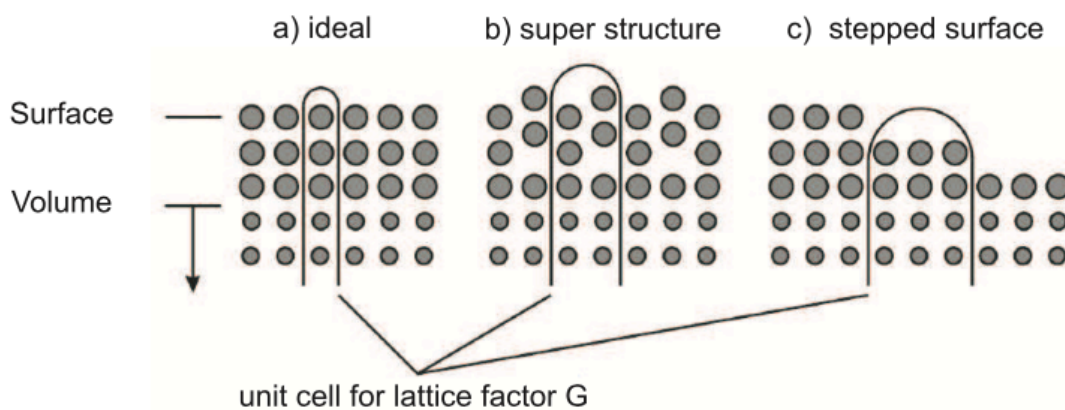
Fig 2.9: Schematic representation of different types of surfaces where the unit cells are taken as columns for study [25].

13

Hence, kinematic approximation is used in this field. In kinematic theory of diffraction, the surface is divided into columns of unit cells extending into bulk as seen in (Fig 2.9) [26]. Hence, only interference of waves scattered at different columns is considered.

Fraunhofer approximation is another assumption where the waves at a great distance from their source are seen as plane waves. The condition is that the distance between the detector and sample has to be much larger than the atomic distance [27]. The diffraction from surface is considered to be the sum of electron wave functions scattered from the initial wave vector $\vec{k}_i$ of the incoming electron to the final wave vector $\vec{k}_f$ by all surface atoms being in columns with positions $\vec{r}(n)$ [28]. The wave function of a surface scattered electron is given as,

$$\psi(\vec{K}, \vec{k}_i) = \frac{1}{N} \sum_n \psi_n e^{i\vec{K}\vec{r}(n)} \tag{2.14}$$

In (Eqn. 2.14) the wave function is the sum of ψ_n which is the scattering amplitude from the n-th unit cell (including also subsurface atoms due to the column approximation) of the surface $\vec{r}(n)$. N is the appropriate normalisation and the scattering vector is $\vec{K} = \vec{k}_i - \vec{k}_f$. The above mentioned scattering amplitude ψ_n of a unit cell $E(n)$ is given as,

$$\psi_n = \sum_{\nu \in E(n)} f_\nu e^{i\vec{K}\vec{r}(\nu)} \tag{2.15}$$

where f_ν is the atomic form factor and the sum runs over all atoms being in one unit cell at positions $\vec{r}(\nu)$. Since the wave function $\psi(\vec{K}, \vec{k}_i)$ could not be measured experimentally, the diffraction phenomena with the diffraction spot intensity is considered and given as,

$$I(\vec{K}, \vec{k}_i) = |\psi(\vec{K}, \vec{k}_i)|^2 = \frac{1}{N^2} \sum_n \sum_m \psi_n \psi_m^* e^{i\vec{K}[\vec{r}(n) - \vec{r}(m)]} \tag{2.16}$$

According to kinematic diffraction theory, the atomic form factor of all columns is considered to be equal. In that case (Eqn. 2.16) could be simplified to (Eqn. 2.17) since the base is assumed to be composed of just one atom [27].

14

The atomic configurations are different at the step edge of the unit cell columns. This shows that at the step edge the structure factor *f* deviates from its average value, this can be seen in (Fig 2.10).
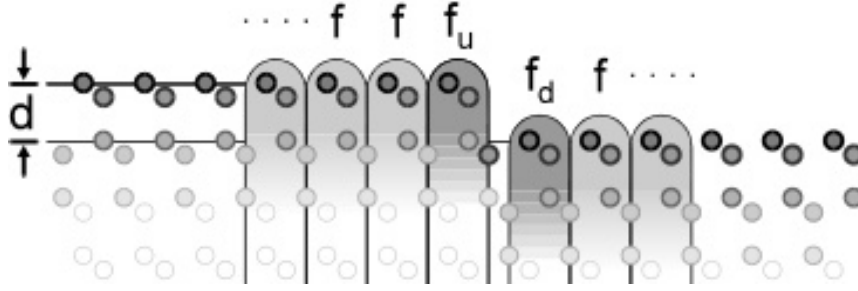

Fig 2.10: Illustration of an atomic step edge with the structure factor *f* deviating from its average value. f_u and f_d show different scattering amplitudes and scattering phases for columns close to the atomic step. *d* is the layer spacing or step height [28].

The different form factors f_u and f_d are a secondary effect often neglected. The modified form factors produce diffuse scattering due to inhomogeneities. The major effect of atomic steps is caused by the different heights of the adjacent terraces causing phase shifts for waves scattered by the upper and by the lower terrace. This causes the splitting into central peak and diffuse shoulder with periodic variation with respect to $\sqrt{E}$ [28]. The splitting of intensity into form factor (=structure factor) and lattice factor is pretty general. It is not related to atomic steps. It is given as,

$$I(\vec{K}, \vec{k}_i) = F(\vec{K}, \vec{k}_i)G(\vec{K}) \tag{2.17}$$

where $\vec{K}$ is the scattering vector, $\vec{k}_i$ denotes the wave vector of the incoming electron and the form factor depends on initial and final wave vector,

$$F(\vec{K}, \vec{k}_i) = |f(\vec{K}, \vec{k}_i)|^2 \tag{2.18}$$

The form factor gives the intensity along the lattice rods and the lattice factor of rough surfaces is determined only by the surface morphology $h(n)$ and scattering vector $\vec{K}$,

$$G(\vec{K}) = \frac{1}{2\pi} \left| \sum_n e^{ia\vec{K}_\parallel n} e^{idK_\perp h(n)} \right|^2 \tag{2.19}$$

The lattice factor does not modify the integral intensity of the spots. The intensity distribution in reciprocal space is influenced by lattice factor. Perfect sharp diffraction spots appear for perfectly

smooth flat surface. In the case of a rough surface, there is a redistribution of intensity from the fundamental diffraction spots [28-30].

2.3.2 Atomic steps

Surfaces are prone to have defects. These influence the scattering behaviour or broadening of reflex profiles. One such defect is called atomic steps where the electrons get backscattered at different terraces. The electrons scattered from terraces are separated by atomic steps with a phase difference of $2\pi S$, that is a path difference given by the product of the scattering phase S and wavelength of the electron λ as seen in (Fig 2.11). The scattering phase S is given as,

$$S = K_{\perp}d/2\pi \qquad (2.20)$$

The incidence angle θ is part of the path difference $S\lambda_{el}$ as shown in (Eqn. 2.21) [28]. The scattering phase S describes the phase difference in numbers of electron wavelength $\lambda_{electron}$ when electrons are scattered from adjacent terraces with a height difference of one atomic step d as illustrated in (Fig 2.11) [28].

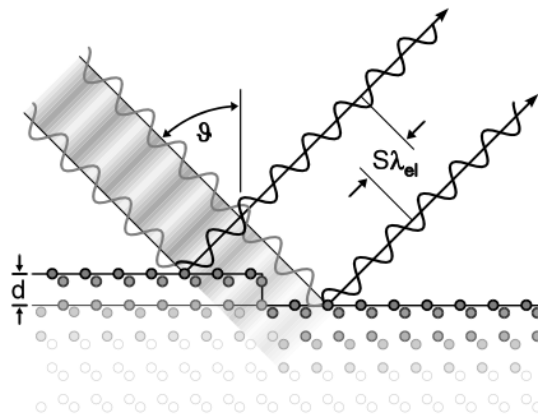Constructive interference of electrons for integer values of S is the Bragg or in-phase condition of scattering.

Fig 2.11: Shows the phase contrast at a step edge. The incidence angle θ is part of the path difference $S\lambda_{el}$ as shown in (Eqn. 2.21) [28]

This is the reason for appearance of a sharp LEED spot of electrons with energy corresponding to a Bragg condition. This condition is not sensitive to any surface roughness. Whereas when electrons interfere destructively, it is the out-of phase or anti-Bragg condition and has a maximum sensitivity to surface roughness. Here, the electrons are redistributed around the sharp LEED spot as a diffuse

16

shoulder. This appears to be a broadened spot and this profile shape could be determined by the lattice factor $G(\vec{K})$. Lattice factor is the two-dimensional Fourier transform of the phase correlation [31]. The surface profile $h(n)$ depends on both the terrace size distribution and the layer height distribution and thus, the information of surface defects can be obtained from the lattice factor [32]. In addition, the terrace size distribution can be deduced directly from the spot profile at out-of-phase conditions.

The (00)-spot that is $K_{\parallel} = 0$ and an arbitrary incidence angle θ the scattering phase S depends on electron wavelength as follows [28],

$$S = 2dcos\theta/\lambda_{electron} \tag{2.21}$$

or electron energy,

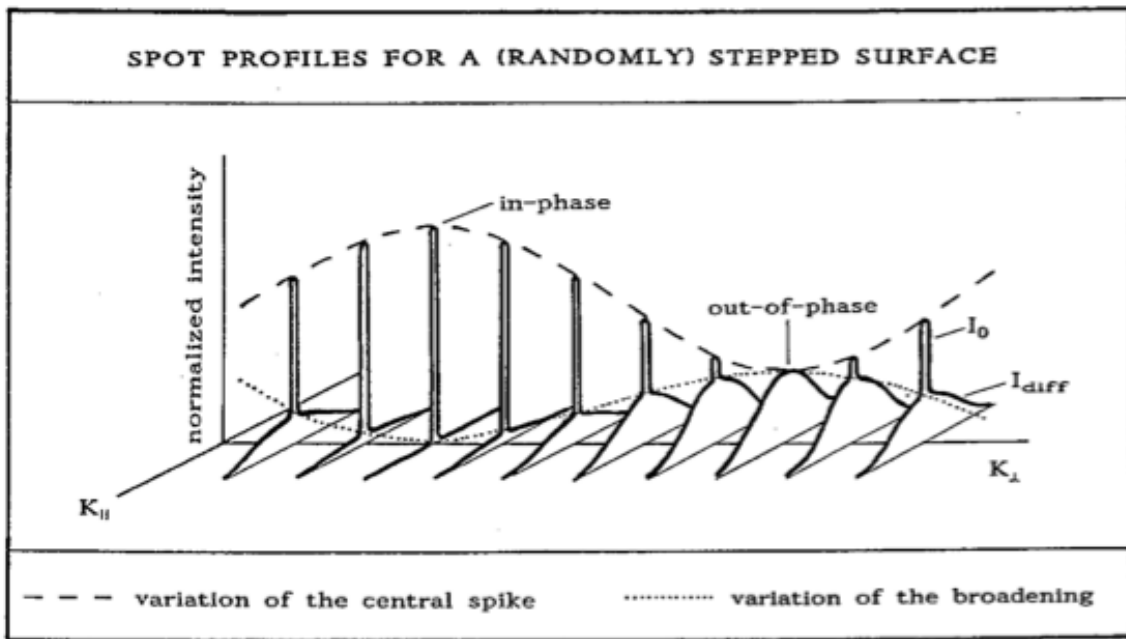$$S = 2dcos\theta\sqrt{E/150.4(eV)} \tag{2.22}$$

Fig 2.12: Illustration of the spot splitting into a central peak and a broad shoulder due to diffraction from rough surfaces. At the in-phase condition, there is only a central peak, while at the out-of-phase condition, there is a broad shoulder [32]

17

2.3.4 Surface morphology

Inhomogeneities at the surface produce an additional broadening of the diffraction spots [33]. The spots of a rough surface consist of a sharp central spike $I_0(K_\perp)$ surrounded by a broadened shoulder $I_{diff}(K_\perp, K_\parallel)$ as shown in (Fig 2.12). The reason for this is that the lattice factor is split into a central part $G_{ideal}(K_\parallel)$ and a diffuse profile. Due to the interference of the electron waves both vary with vertical component of the scattering vector $K_\perp$ in anti-phase, at the in-phase condition there is only the central spike and at the out-of-phase condition the broadening gets its maximum [32].

As mentioned in [34], the experiment is limited to recording intensities, so the lattice factor $G(S)$ value is determined as the proportion of the integral peak over the total intensity (peak and shoulder).

$$G(S) = \frac{\int_{BZ} d^2\vec{K}_\parallel \cdot I_{Peak}(\vec{K}_\parallel)}{\int_{BZ} d^2\vec{K}_\parallel \cdot I_{Peak}(\vec{K}_\parallel) + \int_{BZ} d^2\vec{K}_\parallel \cdot I_{Shoulder}(\vec{K}_\parallel)} \tag{2.23}$$

In the case of two-dimensional peaks, it can be approximated as,

$$\int_{BZ} d^2\vec{K}_\parallel \cdot I(\vec{K}_\parallel) \approx I_{max} \cdot FWHM^2 \tag{2.24}$$

where I_{max} is the maximum peak intensity and FWHM is full width at half maximum.

From the FWHM of the $G(S)$ curve at in-phase conditions the asperity height Δ is determined. The asperity height that is the rms (root mean square) value of the vertical roughness is given as [32],

$$\Delta^2 = d^2 \left[\left\langle h^2(m) \right\rangle - \left\langle h(m)^2 \right\rangle \right] \tag{2.25}$$

(Eqn. 2.25) can be determined by the curvature of the $G(S)$-curve at the in-phase condition. A Gaussian shape is assumed for the $G(S)$-curve as approximation close to the in-phase condition [32],

$$G(S) \approx e^{-\Delta^2(2\pi\delta S)^2} \tag{2.26}$$

with δS as deviation of the scattering phase S from the next integer value and the surface roughness (in the values of the layer distance d) could be evaluated as,

$$\Delta = \frac{1}{2\pi \cdot FWHM} \cdot \sqrt{ln(2) \cdot 150.4} \; [\mathring{A}] \tag{2.27}$$

$G(S)$ contains information about the vertical layer spacing. The step height d is the vertical layer spacing which can be calculated from the central peak and broad shoulder. The formula is given as,

$$d = \frac{1}{2 \cdot \Delta\sqrt{E}} \cdot \sqrt{150.4} \ [\mathring{A}] \tag{2.28}$$

where $\Delta\sqrt{E}$ is the corresponding energy.

The terrace distribution can be determined from the diffuse shoulder fitted with a Lorentzian profile. Knowing only the halfwidth of spots at the out-of-phase condition, the average terrace width could be calculated [35]. This is given as,

$$\langle\Gamma\rangle_{\mathring{A}} = \sqrt{2^{2/3} - 1} \cdot \frac{a \cdot 100\,\%\,BZ}{\pi} \cdot \frac{2}{FWHM_{\%BZ}} \tag{2.29}$$

where a is the lattice constant.

However, it can only be used if the broadening has Lorentzian shape. It cannot be used for the ring-like shoulders [31, 36].

The two most important parameters characterising the terrace size distribution are the average terrace size $\langle\Gamma\rangle$ and the standard deviation σ. These influence the characteristic parameters of the spot profile that is spot splitting and satellite half-width. The scaled standard deviation $\sigma/\langle\Gamma\rangle$ of the terrace size distribution can be determined from the ratio of spot splitting and satellite half-width. The spot profile analysis of the splitting of diffuse shoulder into two Lorentzian functions (a ring-like structure) is based on two parameters, the satellite position $K^{(0)}$ and half-width κ.

To analyse spot profiles with half-width [31],

$$\kappa = \frac{\pi^2}{2\langle\Gamma\rangle} \cdot \left(\frac{\sigma}{\langle\Gamma\rangle}\right)^2 \tag{2.30}$$

and spot position,

$$K^{(0)} = \frac{\pi}{\langle\Gamma\rangle}\left[1 - \frac{\pi^2}{6}\left(\frac{\sigma}{\langle\Gamma\rangle}\right)^4\right] \tag{2.31}$$

(Eqn. 2.30) and (Eqn. 2.31) are only valid for $\sigma/\langle\Gamma\rangle < 0.6$. The $\sigma/\langle\Gamma\rangle$ can be determined from the analytical results of (Eqn. 2.30) and (Eqn. 2.31) for sharp satellite profiles. However, in the case of $\sigma/\langle\Gamma\rangle > 0.6$ the full width at half maximum (FWHM) is almost constant while the spot splitting decreases nearly linearly with increasing $\sigma/\langle\Gamma\rangle$ (Fig 2.13).

Thus, the standard deviation can be obtained from the ratio of spot splitting and FWHM (dots) as shown in the (Fig 2.13), the average terrace width can be derived from the half-width of the spots. In addition, the results and analysis from [31], shows that in the case of a no-ring and with only single Lorentzian fitting, the same formula of a ring-like structure can be used (Eqn. 2.29).
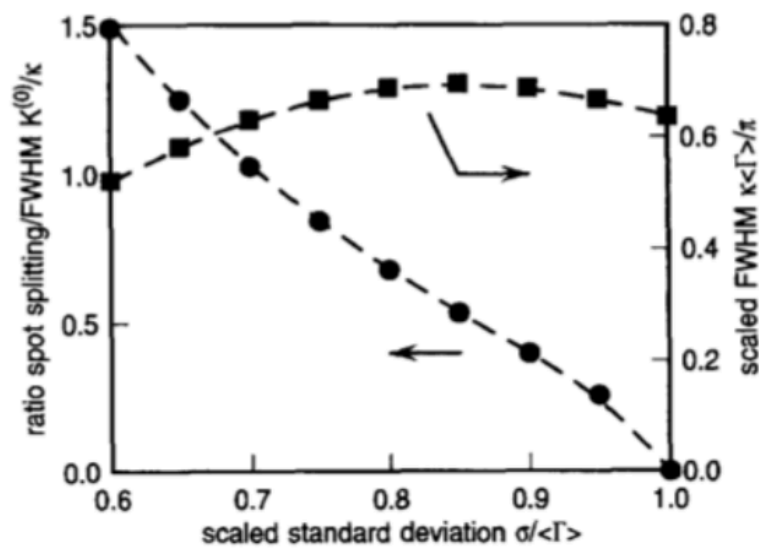

Fig 2.13: Illustration of the spot splitting (dots) and half-width (squares) of the shoulders obtained from fitting two Lorentzians. The ratio of spot splitting and FWHM determines the standard deviation. The dashed lines show the behaviour of $\sigma/\langle\Gamma\rangle$. The figure is taken from [31]

In addition, peaks formed at in-phase condition of diffuse shoulder are due to inhomogeneities and the average terrace width $\langle\Gamma\rangle$ could be interpreted as domain size D (i.e.) $\Gamma = D$.

2.3.5 Mosaics

Mosaics are crystallites connected by small angle grain boundaries (Fig 2.14). They are one of the types of defects on surface. They often arise in heteroepitaxial systems. Since the normal orientation of the crystallites are inclined by small angles, the diffraction rods follow mis-orientation.
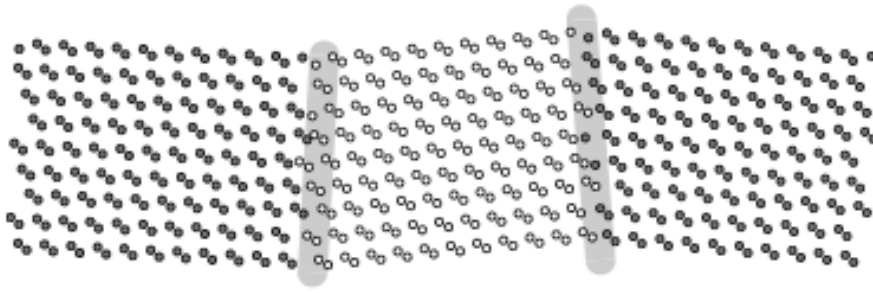
Fig 2.14: Illustration of small angle mosaics [28].

The diffraction pattern must be constructed by the incoherent sum of the single crystal patterns of each of the crystallites. (Fig 2.15) shows the mosaic with preferred orientations in reciprocal space along $\vec{K}_{\perp}$. The mosaic angle is denoted as θ.
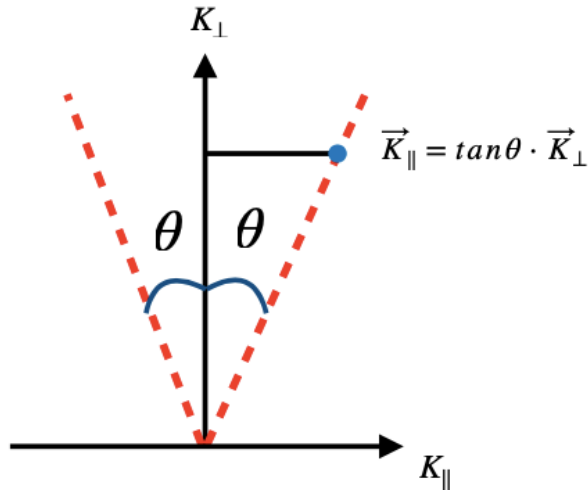

Fig 2.15: Shows the mosaic angle θ of the mosaic rods (dash lines) at two distinct orientations along $\vec{K}_{\perp}$ in reciprocal space. This leads to the increase in broadening of spots.

In (Fig 2.15) the mosaic angle θ from the diffraction rod increases linearly along $\vec{K}_{\perp}$. This mosaic angle θ could be calculated from the peak position,

$$\vec{K}_{\parallel} = tan\theta \cdot \vec{K}_{\perp} \tag{2.32}$$

$$\vec{K}_{\perp} = 2k \tag{2.33}$$

with wavevector,

$$k = |\vec{k}_i| = |\vec{k}_f| \tag{2.34}$$

21

and

$$k = \frac{\sqrt{2m_e E}}{\hbar} \tag{2.35}$$

$$\vec{K}_{\parallel}[BZ\%] = m\sqrt{E} \text{ with } m = 200\% \cdot tan\theta \cdot \frac{\sqrt{2m_e \cdot a}}{h} \tag{2.36}$$

and thus,

$$\vec{K}_{\parallel}[BZ\%] = 200\% \cdot tan\theta \cdot \frac{\sqrt{2m_e \cdot a}}{h} \cdot \sqrt{E} \tag{2.37}$$

where h is the Planck's constant, a is the lateral lattice constant and m_e is the electron mass.

2.3.6 Instrumental broadening

There is instrumental broadening due to the finite resolution of SPA-LEED apparatus. Hence, there is no possibility of an infinitely sharp reflex profile of an ideal smooth surface. The instrument is not so perfect. In order to get accurate results, this broadening has to be considered in the analysis of the reflex profiles [26].

The instrument function can often be approximated by a gaussian function. The instrumental broadening can be determined by measuring the smooth surface at in-phase conditions [34]. However, the spot profile can also be influenced by other surface defects such as mosaics. Thus, the FWHM at in-phase gives some "effective" instrumental broadening including instrument and surface with defects (except atomic steps). Transfer range is the instrumental limit of detection of structures which is influenced by sample imperfections [37]. It is given as,

$$t = a\frac{K_{10}}{H_t} = \frac{2\pi}{H_t} \tag{2.38}$$

where H_t is the full width at half maximum of central peak at in-phase condition. K_{10} is the distance between two diffraction reflections and a is the lattice constant. Therefore, the transfer width also known as the correlation length could be given as,

$$t = \frac{100\,\%}{FWHM[\%BZ]} \cdot a \tag{2.39}$$

3 Material system

This chapter describes the structural and physical properties of the material used to study in this master thesis.

3.1 Strontium titanate

At room temperature, $SrTiO_3$ crystallises in the ABO_3 cubic perovskite structure. It has a lattice constant of $a_{SrTiO_3} = 3.905\text{Å}$ and an atomic density of $\rho = 5.12 \text{ g} / cm^3$ [38].

The schematic structure of the crystal is shown in (Fig 3.1). The Ti^{4+} ions are at the centre like a body centred cube, six-fold coordinated by O^{2-} ions, which are face centred. Each of the Sr^{2+} ions is surrounded by four TiO_6 octahedra. Therefore, each Sr^{2+} ion is coordinated by 12 O^{2-} ions and are located on the corners of the cube [39].

[001]

perovskite structure

Ti^{4+}

Sr^{2+}

O^{2-}

$a_{SrTiO_3} = 3.905 \text{ Å}$
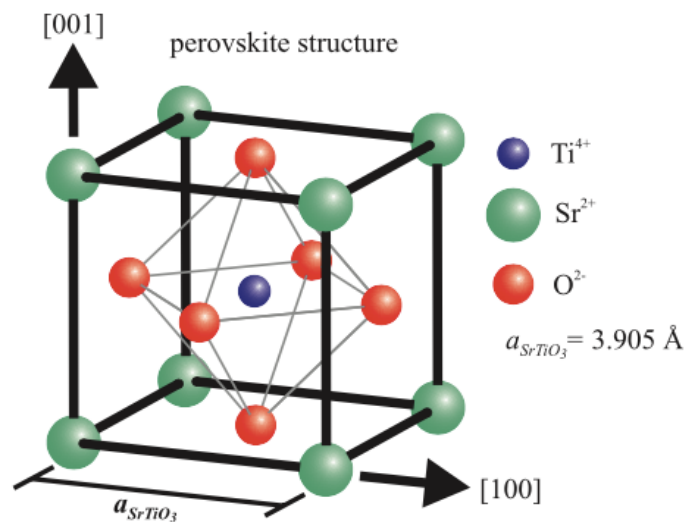
[100]

a_{SrTiO_3}

Fig 3.1: An illustrative representation of the cubic unit cell of $SrTiO_3$. The sizes of the spheres representing the atoms are arbitrary.

STO has an indirect band gap of 3.25 eV [39, 40], making it an insulator and thus, it is optically transparent. It has mixed ionic and covalent bonding properties. STO is intrinsically diamagnetic [41]. The STO surface can exhibit two different types of atomic alternating planes. For instance, in the (100) surface, one, formed by a TiO_2 plane and the second by a SrO plane.
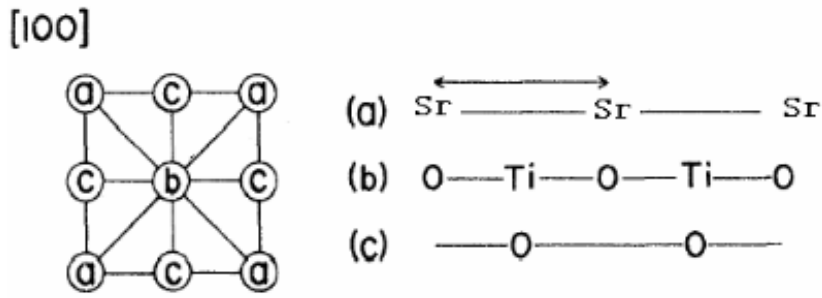
Fig 3.2: Atomic arrangement for the <100> axial direction in STO. The arrangement shown on the left is an end view of the cubic unit cell and the letters refer to the individual rows shown on the right.

The presence of oxygen vacancies or dopants modifies electronic structure and magnetic properties. Doping a material has stronger control of conductivity over oxygen vacancy [42]. For this research work, in order to avoid charging effects during SPA-LEED measurements, the STO substrates are doped with 0.05 wt% Nb. Electron doping is sufficient to make STO a conducting oxide [41].

4 Experimental set-up

In this chapter, the basics of experimental set-up are discussed briefly.

4.1. Ultra high vacuum

The experimental condition for surface science study is to have an Ultra-High Vacuum system (UHV). The reason to maintain a vacuum environment is to conduct the study on clean surfaces, as there is a constant interaction of gas particles with the surface. The rate at which the surface of the sample encounters adsorbates in a regular atmospheric condition is higher compared to a vacuum space. Hence, it is necessary to carry out the experiment in ultra high vacuum system. The settlement of adsorbates could be calculated with Monolayer time.

Monolayer time τ is the time required for a monolayer of adsorbates to deposit on the surface. In principle to the Kinetic theory of gases, monolayer time τ could be evaluated by [43],

$$\tau = \frac{n_0\sqrt{2\pi m k_B T}}{p} \tag{4.1}$$

where n_0 is the number of atoms in a monolayer, m is the molecular mass, T is the temperature and p is the pressure. There is an increase in τ with a decrease in pressure. In comparison to pressures of normal room setup, the pressure in UHV condition is $10^{-10} mbar$ and τ is in the range of 10 hour.

The parts and the arrangement of the experiment is given in (Fig 4.1). The setup comprises of a load lock and a main chamber. They are separated by a valve. The transfer rod is used to move the sample from load lock to the main chamber. The sample is implanted in a manipulator that is present in the main chamber. Due to the bombardment of electrons the sample is heated to a desired temperature with the manipulator. It also plays a vital role in aligning the sample facing SPA-LEED for analysis of surface. Furthermore, the sample could be moved along x, y, z directions. It could be rotated and tilted according to preference.
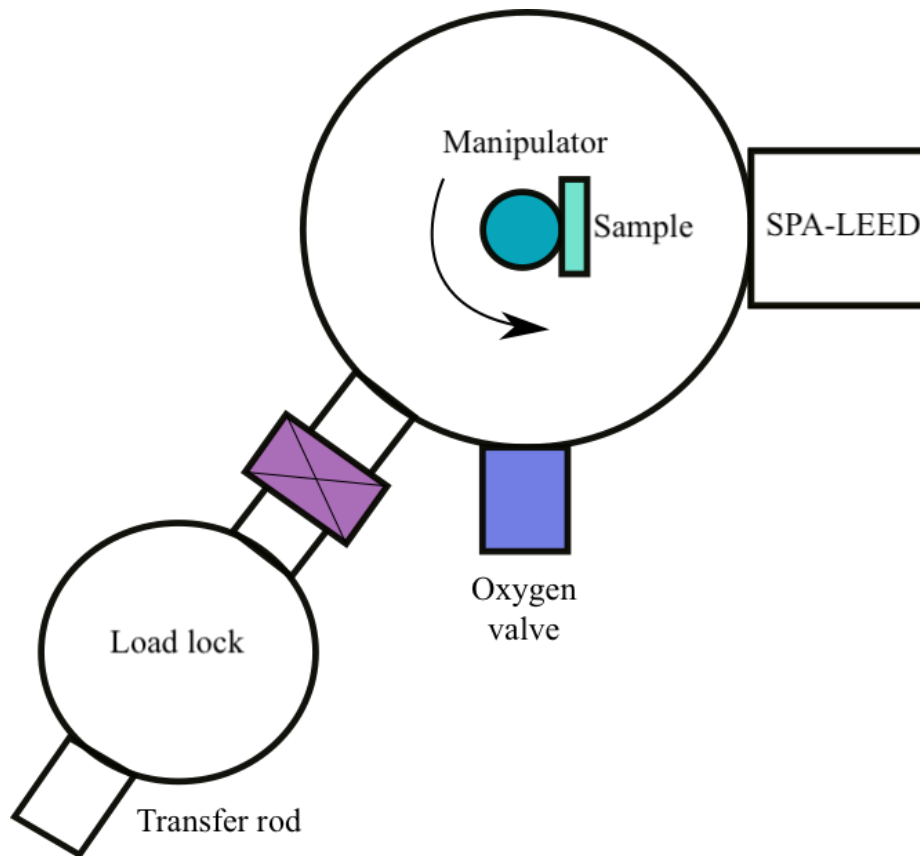
Fig 4.1: Schematic representation of the experimental set-up. Through the load lock, the transfer rod transfers the sample to the main chamber.
It is positioned at the manipulator which moves the sample. SPA-LEED for analysis.

Overall, in order to achieve the desired pressure of $10^{-10}mbar$ in the UHV chamber, a three stage pumping system is used. Beginning with a rotary vane pump which generates a pressure of $10^{-2}mbar$ followed by a turbo molecular pump that sets a pressure of $10^{-8}mbar$. Then with a combined effort of Ion getter pump and Ti sublimation pump the required pressure of $10^{-10}mbar$ in the main chamber is created. The detailed information about the pumps could be found in [17].

4.2. SPA-LEED

This study was carried out using a diffraction technique known as Spot Profile Analysis Low Energy Electron Diffraction (SPA-LEED), it provides high resolution diffraction images.
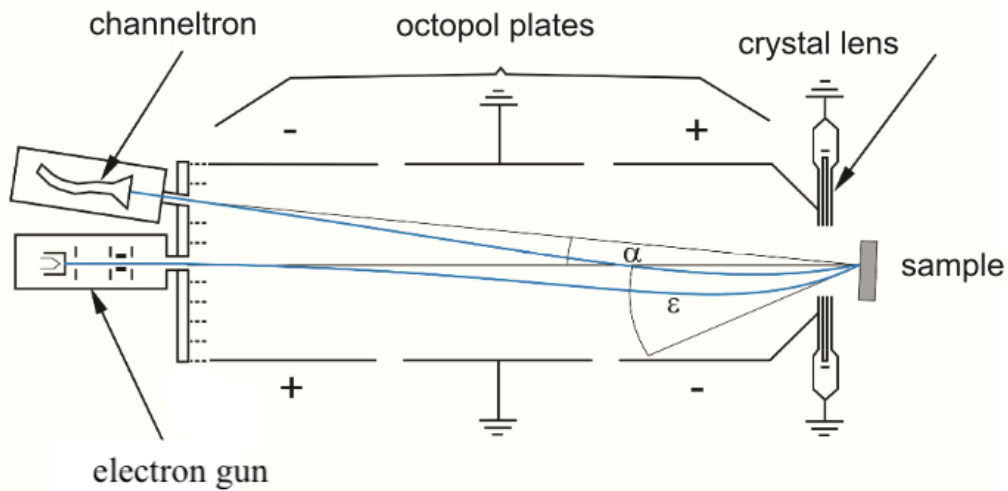
Fig 4.2: Schematic diagram of experimental setup of SPA-LEED. The electron gun is the source which emits electrons that hit the sample. The diffracted beam reaches the detector (channeltron) by passing through octopole plates [44].

SPA-LEED is built with an electron gun which emits electrons at an energy of 20-500 eV as seen in (Fig 4.2). They are accelerated in the direction of the sample with electron source consisting of a cathode filament, an anode, Wehnelt cylinder and electrostatic lenses that collimate the electron beam towards the sample. The focussed beam of electrons pass through 3×8 octopole plates with the middle plates being grounded. The role of octopole plates are to act as a deflection unit. The electron beam is focussed onto the detector by crystal lens. The purpose of a channeltron is to receive the reflected beam which is at an angle α, the fixed angle between the incident and diffracted beam. By varying the voltage applied on octopole plates thereby varying the angle of incidence ε, the reciprocal space could be scanned one by one. Due to construction, the angle α is kept constant. A larger area of k space could be scanned by varying the angle of incidence using SPA-LEED compared to that of a conventional LEED (Chapter 2.3), where wave vector is centred at the origin and terminates at an intersection between a diffraction rod. A point to be noted in a modified Ewald sphere (Fig 4.3) is that the angle between incident and reflected waves namely $\vec{k}_i$ and $\vec{k}_f$ is constant and independent of ε.
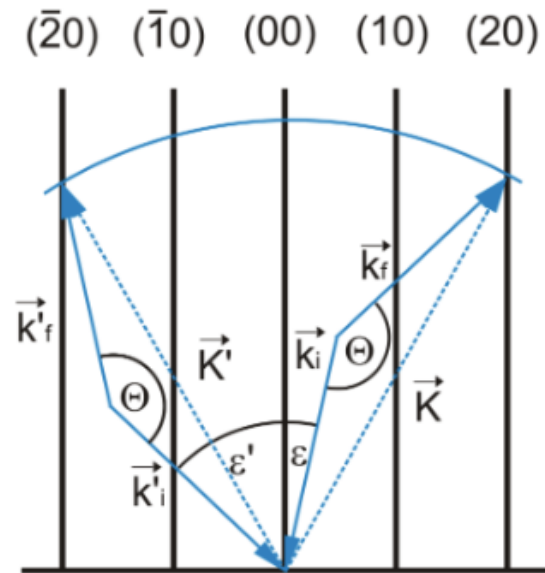
Fig 4.3: Modified Ewald sphere constructed in reciprocal space as in a SPA-LEED. K and K' are scattering vectors, $\vec{k}_i$ and $\vec{k}'_i$ are incident wave vectors for different incident angles. $\vec{k}_f$ and $\vec{k}'_f$ are reflected wave vectors. Taken from [44]

The main difference of SPA-LEED from the conventional Low Energy Electron Diffraction (LEED) is the way of detection. The former uses channeltron for detection while the later detects the diffracted electrons by a screen. As mentioned in (Chapter 1), analysis of spot profiles can give quantitative information like step height and terrace width. LEED is mostly used only for qualitative analysis. The digital recording of the diffracted intensities measured with the channeltron in a SPA-LEED is one reason behind the above statement. In addition, the quality of the electron gun is also important [43].

This research work was carried out by a commercial SPA-LEED from the manufacturer named "Omicron" [34].

4.3. Sample preparation

The sample STO is first cleaned with acetone, distill water and isopropanol. This initial step is done in order to make sure the sample is free of contamination.

The sample is then placed into the UHV chamber where it is annealed at various temperatures in the presence of molecular oxygen at a pressure of $1 \times 10^{-4} mbar$ for 1 hour. High voltage is applied between filament and sample. As a result, the electrons are emitted due to glow-electrical effect/ thermionic emission which is a process of heating by electron bombardment.

At first, the measurement of untreated sample for reference was taken and analysed. The sample was then treated at $400°C$, $600°C$ and $800°C$, respectively, in an oxygen atmosphere of $1 \times 10^{-4} mbar$ for a time period of 1 hour. Afterwards the sample was analysed by SPA-LEED.

5 Discussion and results

This chapter provides the discussion of the data gathered from the experiment. The results are presented as per the discussion.

5.1. Analysis of experimental data

The 2D measurements and line scans were performed by the measurement software *Spaleed_Qt* developed by Henrik Wilkens (University of Osnabrück). The functionality of this computer program is that it helps to do 2D measurements and line scans for the study of our Low energy electron diffraction (LEED) experiment on surfaces. Further analysis of line scans were done using software *Peakorino,* formatted by Jascha Bahlmann (University of Osnabrück).

As discussed in (Chapter 4), the sample preparation was carried out in ultra high vacuum chamber with an oxygen pressure of $1 \times 10^{-4} mbar$ for 1 hour. The aim was to study different cleaning conditions of the substrate STO ($SrTiO_3$), in the pressure of molecular oxygen at various temperatures. The following subchapters showcase the respective results and discussion of SPA-LEED experiments performed at UHV conditions.

2D measurements were done for energy ranges of 100 eV, 120 eV, 140 eV, 160 eV, 180 eV and 200 eV. This was followed by line scan for an energy range of 70-200 eV at steps of 2 eV with a length of 20%BZ. This particular analysis of the (00) reflection led into the splitting of a central spike and diffuse broad shoulder. The oscillation of full width at half maximum (FWHM) with the electron energy results in the presence of defects (atomic steps, inhomogeneities etc.) on the surface of the substrate.

(Fig 5.1) shows 2D scans of SPA-LEED on STO (001) surface and the images of diffraction pattern of sample's surface at 100 eV of different preparation temperatures.
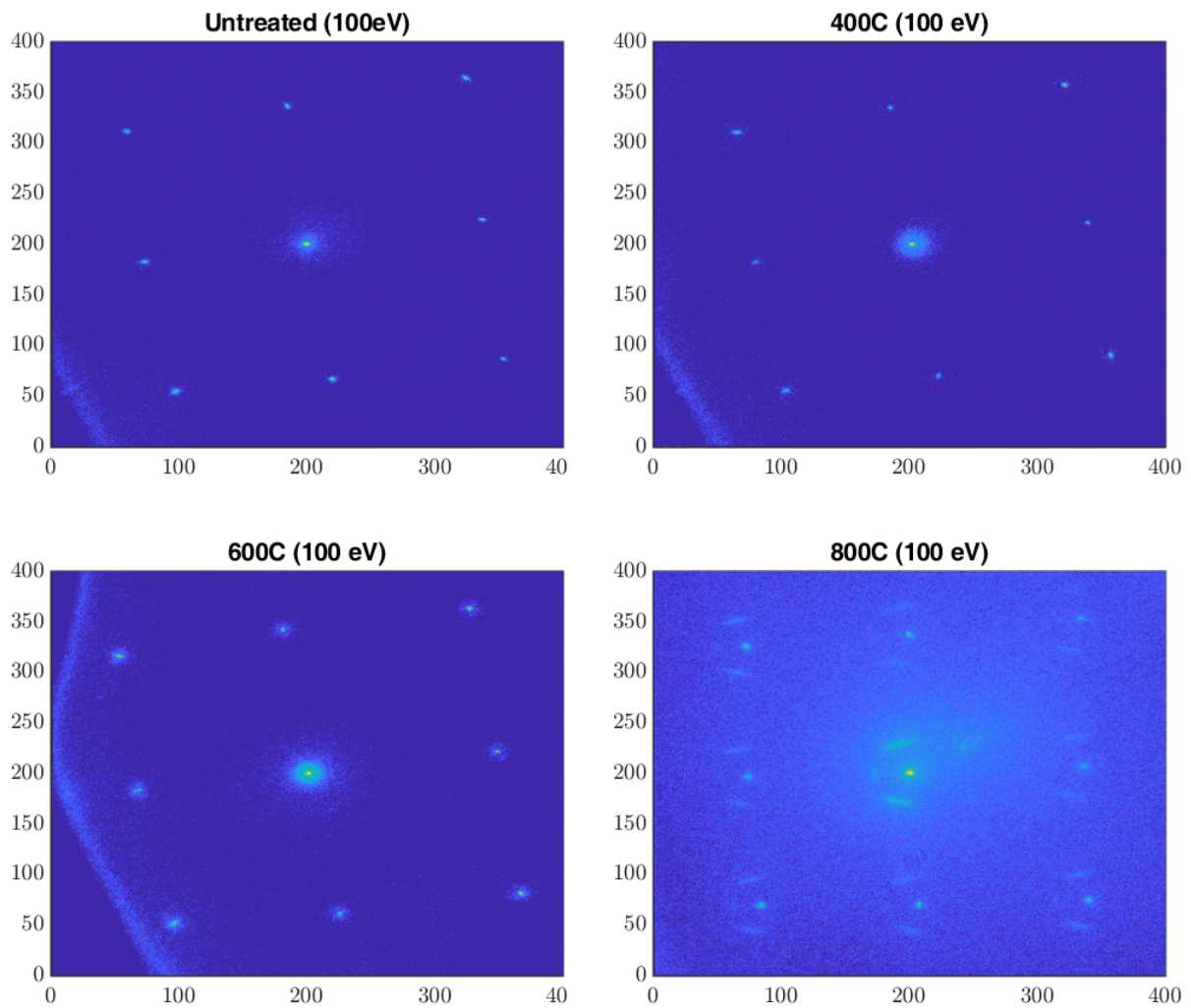
Fig 5.1: Selective 2D scans of SPA-LEED on STO (001) surface. Images show the diffraction pattern of the sample's surface at 100 eV of different preparation temperatures ($20°C$, $400°C$, $600°C$, $800°C$)

5.2. Results of untreated sample

In Peakorino, the untreated sample's data points were fitted with two Lorentzian functions, a broad shoulder and a central peak (Fig 5.2). Data from the fitted profile was extracted to calculate and analyse the surface morphology like step height (d), terrace width $\langle \Gamma \rangle$ and surface roughness (Δ).
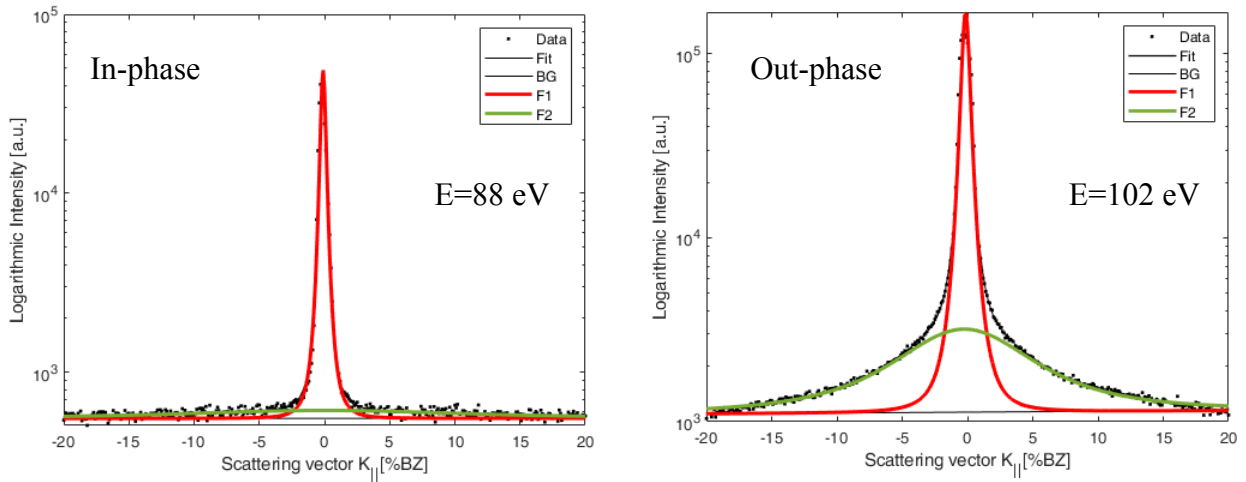
Fig 5.2: Splitting of (00) reflex into a broad shoulder and a peak. The plot shows the data points fitted with two Lorentzian functions

(Fig 5.3) shows the full width at half maximum (FWHM) of broad shoulder against square root of energy. The oscillatory behaviour in the plot with maxima and minima at in-phase and out-of-phase conditions is observed. The step height of STO was found with the analysis of scattering phases according to (Eqn. 2.28). As a result, the step height of STO was calculated to be (3.91 ± 0.02) Å. The literature value of STO is 3.905 Å. Thus, within experimental uncertainties, the value from experiment agrees well with the value reported in literature.
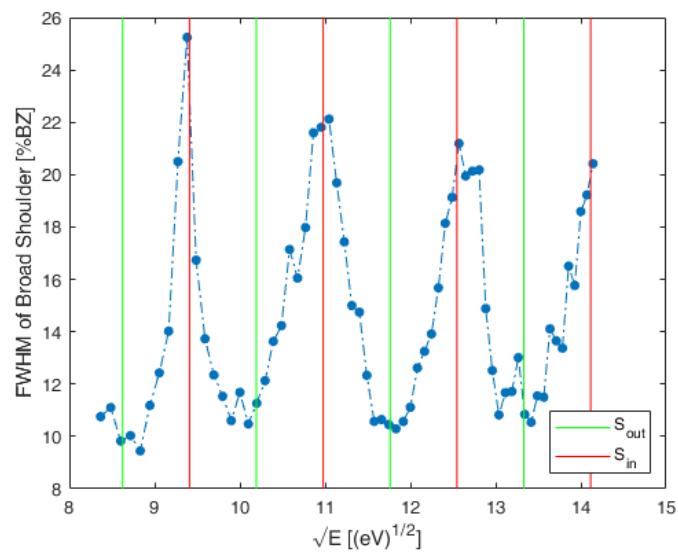

Fig 5.3: FWHM of broad shoulder with in-phase and out-of-phase conditions

From (Fig 5.3), it is seen that the minima with a FWHM of $(10.6 \pm 0.5)\,\%\,BZ$ are at out-of-phase conditions. With respect to (Eqn. 2.29) and with FWHM, the average terrace width $\langle \Gamma \rangle$ from the broad shoulder is deduced to be (18.0 ± 0.5) Å. The (Fig 5.3) also shows that the maxima with a FWHM of $(22.1 \pm 1)\,\%\,BZ$ are at in-phase conditions. There is a strange behaviour of the FWHM of the shoulder and as mentioned in (Chapter 2.3.4), peaks formed at in-phase condition are due to inhomogeneities and, here, the attributed average domain size D is (8.6 ± 1) Å.

(Fig 5.4) shows the full width at half maximum (FWHM) of the central peak against square root energy. The oscillatory behaviour with maxima and minima at out-of-phase and in-phase conditions is observed in the plot and the step height (d) could be concluded.
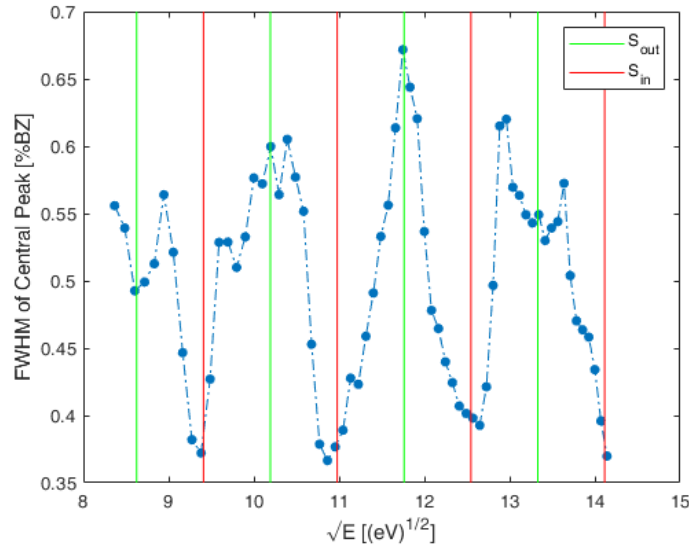

Fig 5.4: FWHM of central peak with in-phase and out-of-phase conditions

The step height of STO was found with the analysis of scattering phases according to (Eqn. 2.28). As a result, the step height (d) of STO was calculated to be (3.91 ± 0.02) Å being in accordance with the literature value of STO 3.905 Å with experimental uncertainties. From (Fig 5.4), it is seen that the in-phase condition is at minima with a FWHM of $(0.39 \pm 0.01)\,\%\,BZ$. With respect to (Eqn. 2.39), the transfer width is calculated to be $(100 \pm 0.1)\,nm$.

(Fig 5.5) shows lattice factor G(S) against square root energy. The lattice factor G(S) was calculated from the (Eqn. 2.23). The periodic oscillations of the lattice factor with scattering phase is a result of the presence of steps. In accordance with the former analysis of FWHM, the step height (d) of STO is calculated to be (3.91 ± 0.02) Å from (Eqn. 2.28) being in accordance with the

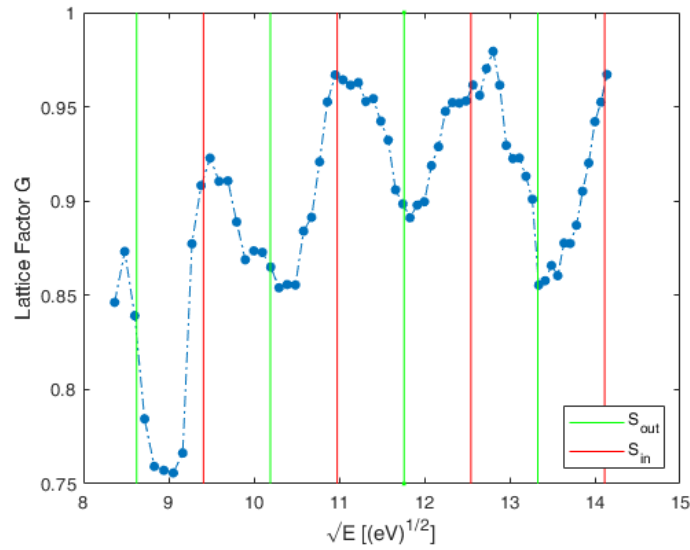literature value of STO 3.905 Å with experimental uncertainties.

Fig 5.5: Lattice factor G with in-phase and out-of-phase conditions

The (Fig 5.5) shows the maxima and minima are at in-phase and out-of-phase conditions respectively. The $G(S)$ value reaches an average maximum of (0.95 ± 0.02) and does not go to 0 which means that the shoulders don't completely disappear at the in-phase condition and central peaks don't vanish at the out-of-phase condition. This could be because of defects such as inhomogeneities and atomic steps, respectively.
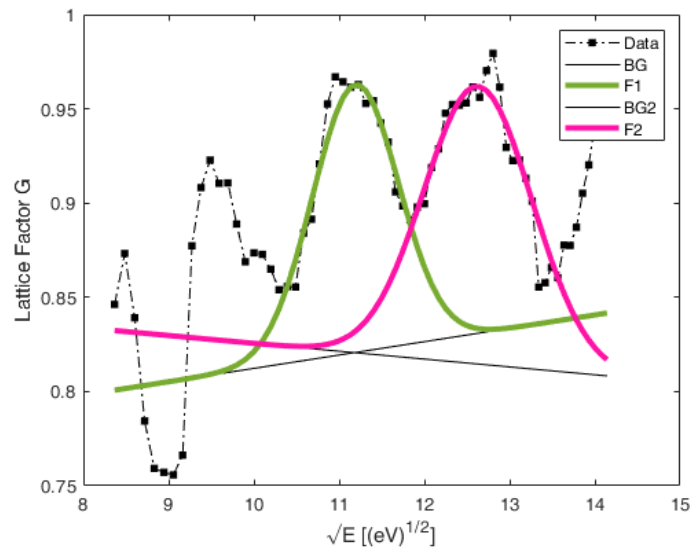

Fig 5.6: The two in-phase conditions of lattice factor G approximated with a Gaussian function to estimate the surface roughness from their FWHM

The (Fig 5.6) shows peaks of $G(S)$, fitted with gaussian functions. The values of FWHM of the respective peaks were applied in (Eqn. 2.27) and the surface roughness (Δ) is found to be (1.23 ± 0.01) Å. The variation of surface roughness with respect to change in temperature is discussed in (Chapter 5.6).

5.3. Results of sample treated at 400°C

After annealing at $400°C$ in $1 \times 10^{-4} mbar\ O_2$ for 1 hour, the spot profiles show a central peak and ring-like shoulders. In Peakorino, the data points were fitted with three Lorentzian functions, using one Lorentzian for the central peak and two Lorentzians for the ring-like broadening (Fig 5.7). The parameters of two Lorentzians describing the ring-like broadening (FWHM and intensity) were coupled.
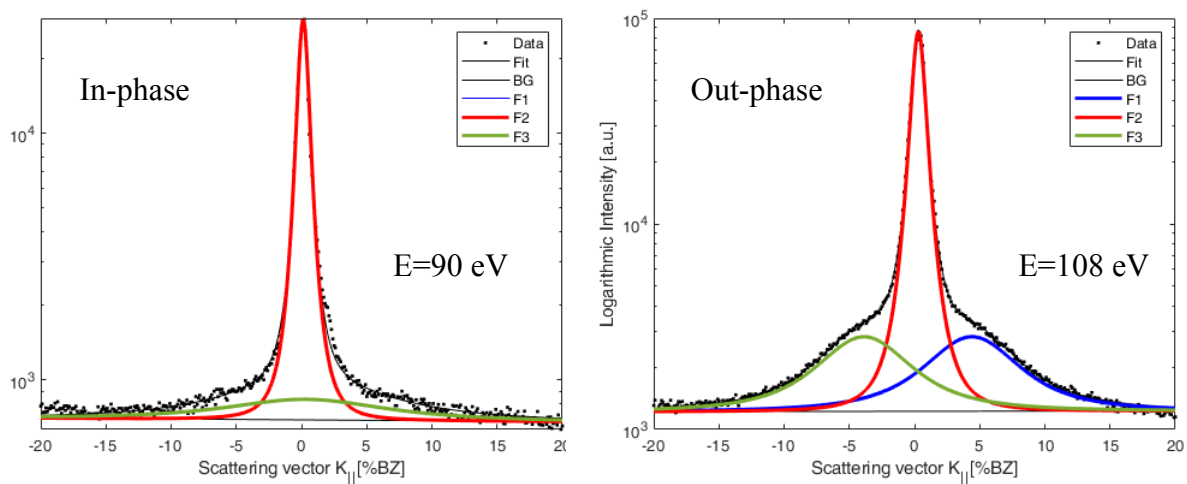

Fig 5.7: Splitting of (00) reflex showing a ring-like broadening and a peak. The plot shows the data points fitted with three Lorentzian functions

(Fig 5.8) shows the full width at half maximum (FWHM) of one Lorentzian of the ring-like shoulder against the square root of energy. The oscillatory behaviour in the plot with maxima and minima at in-phase and out-of phase conditions is observed and the step height (d) could be concluded. The step height of STO was found with the analysis of scattering phases according to (Eqn. 2.28). As a result, the step height (d) of STO was calculated to be (3.95 ± 0.05) Å being in accordance with the literature value of STO is 3.905 Å within the experimental uncertainties.
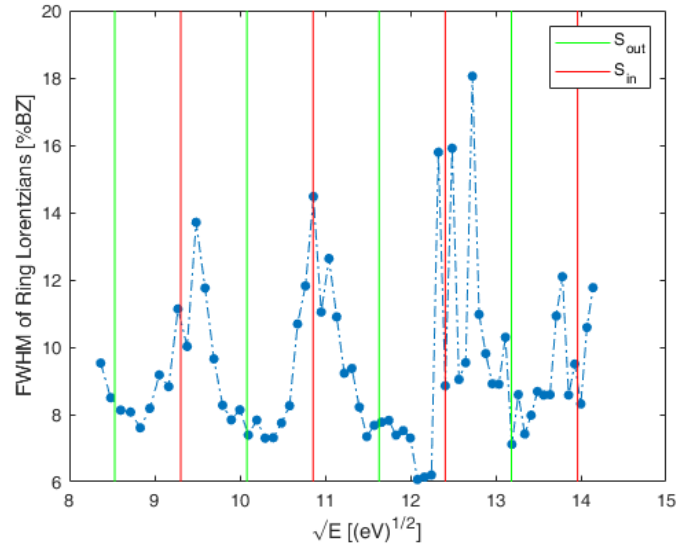
Fig 5.8: FWHM of ring Lorentzians with in-phase and out-of-phase conditions

The terrace width cannot be calculated only from the FWHM of the ring Lorentzians. Hence, the diameter of the ring is taken into account. As mentioned in (Chapter 2.3.4), the standard deviation $\sigma/\langle\Gamma\rangle$ can be obtained from the ratio of spot splitting and FWHM. At out-of-phase condition, the ring diameter is $8\,\%\,BZ$ (Fig 5.10) and FWHM is $8\,\%\,BZ$ (Fig 5.8) thus the ratio of $2K_o/FWHM$ is 1.
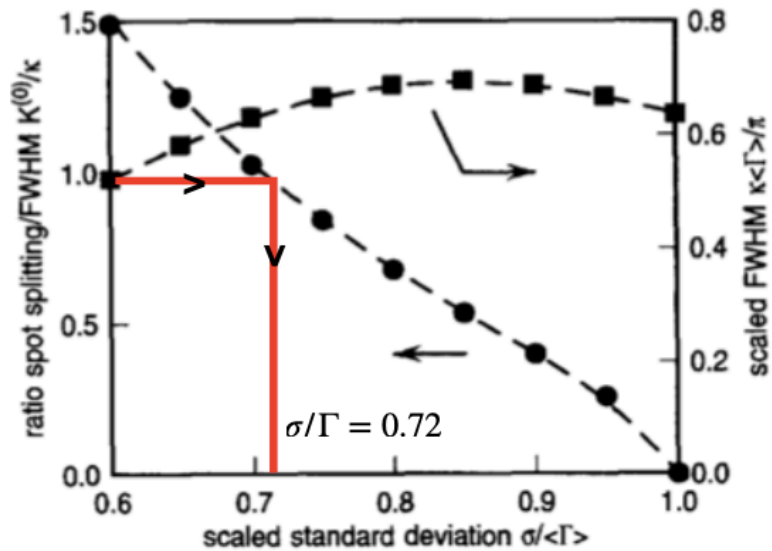

Fig 5.9: The red line shows the estimated standard deviation $\sigma/\langle\Gamma\rangle = 0.72$ obtained from the ratio of spot splitting and FWHM of ring Lorentzians. The plot is taken from [31] and compared to the experimental results of this thesis. In the case of a no-ring, single Lorentzian, $\sigma/\langle\Gamma\rangle = 1$

39

As per the results from [31], it is seen that when the ratio of spot splitting and FWHM is 1 then $\sigma / \langle \Gamma \rangle$ is 0.72 (Fig 5.9), thus supporting the experimental result. In addition, as stated in [31], the average terrace width can be evaluated from the half-width of ring Lorentzian and the same formula for the no-ring and single Lorentzian can be used. In the case of a no-ring structure with only single Lorentizian like in (Chapter 5.2 and 5.5), the standard deviation $\sigma / \langle \Gamma \rangle = 1$ is as seen in (Fig 5.9) .
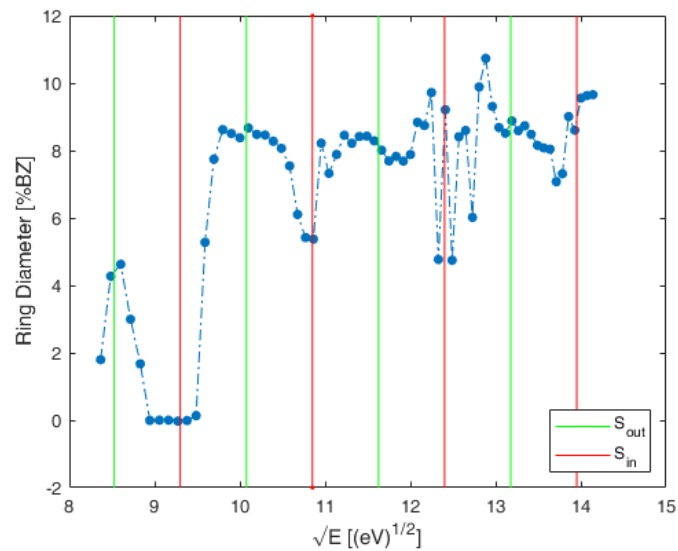

Fig 5.10: Ring diameter with in-phase and out-of-phase conditions

From (Fig 5.8), it is seen that the out-of-phase condition is at minima with a FWHM of (7.8 ± 0.1) $\% BZ$. With respect to (Eqn. 2.29) and with FWHM, the average terrace width $\langle \Gamma \rangle$ from the broad shoulder is deduced to be (24.3 ± 0.01) Å. The (Fig 5.8) also shows that the maxima with a FWHM of $(14 \pm 0.1) \% BZ$ are at in-phase conditions. Thus, the average domain size (D) is calculated to be (13.6 ± 0.1) Å.

(Fig 5.11) shows the full width at half maximum (FWHM) of the central peak against square root energy. The oscillatory behaviour with maxima and minima at out-of-phase and in-phase conditions is observed in the plot and the step height (d) could be concluded. The step height of STO was found with the analysis of scattering phases according to (Eqn. 2.28). As a result, the step height (d) of STO was calculated to be (3.95 ± 0.05) Å being in accordance with the literature value of STO 3.905 Å with experimental uncertainties. From (Fig 5.11), it is seen that the in-phase condition is at minima with a FWHM of $(0.8 \pm 0.01) \% BZ$. With respect to (Eqn. 2.39), the transfer width is calculated to be $(48.8 \pm 0.1) \, nm$.
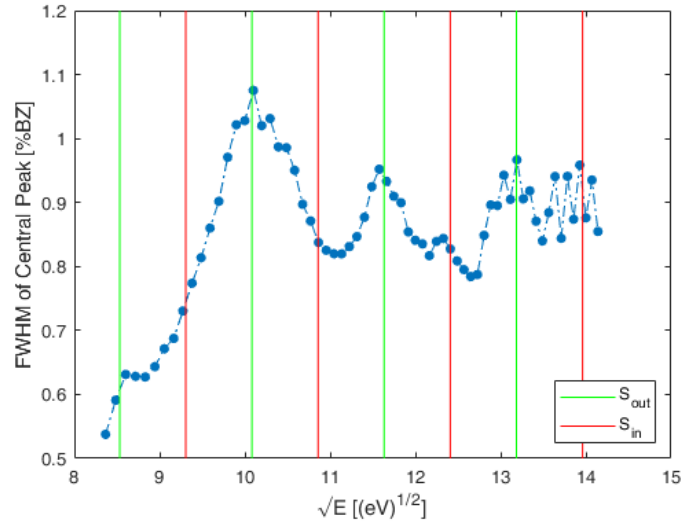
Fig 5.11: FWHM of central peak with in-phase and out-of-phase conditions

(Fig 5.12) shows lattice factor G(S) against square root energy. The lattice factor G(S) was calculated from the (Eqn. 2.23). The periodic oscillations of the lattice factor with scattering phase is a result of the presence of steps. In accordance with the former analysis of FWHM, the step height (d) of STO is calculated to be (3.95 ± 0.05) Å from (Eqn. 2.28) being in accordance with the literature value of STO, 3.905 Å with experimental uncertainties.
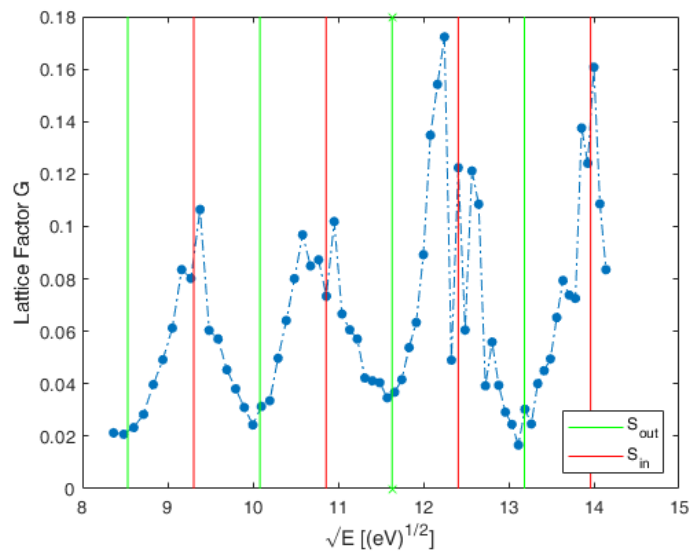

Fig 5.12: Lattice factor G with in-phase and out-of-phase conditions

The (Fig 5.12) shows the maxima and minima are at in-phase and out-of-phase conditions respectively. The $G(S)$ value reaches an average maximum of (0.12 ± 0.02) and does not go to 0 which means that the shoulders don't completely disappear at the in-phase condition and peaks don't vanish at the out-of-phase condition. This could be because of defects such as inhomogeneities and atomic steps, respectively.

The (Fig 5.13) shows peaks of $G(S)$, fitted with gaussian functions. The values of FWHM of the respective peaks were applied in (Eqn. 2.27) and the surface roughness (Δ) is found to be (2.23 ± 0.01) Å. The variation of surface roughness with respect to change in temperature is discussed in (Chapter 5.6).
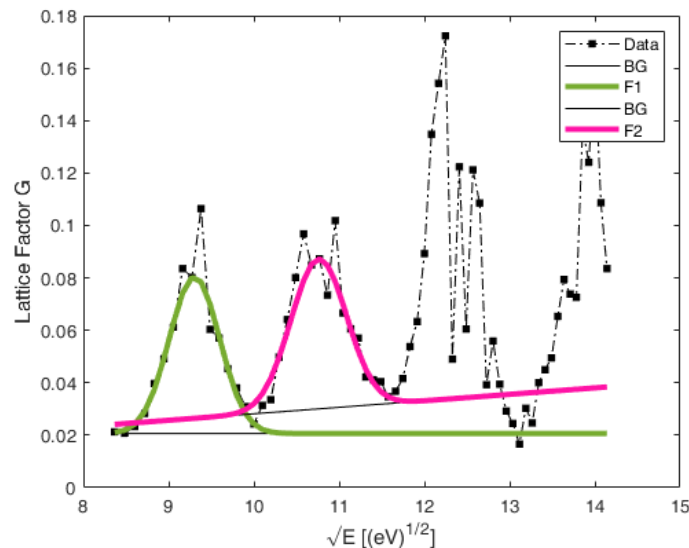

Fig 5.13: The two in-phase conditions of lattice factor G approximated with a Gaussian function to estimate the surface roughness from their FWHM

5.4. Results of sample treated at 600°C

After annealing at $600°C$ in $1 \times 10^{-4} mbar\ O_2$ for 1 hour, the spot profiles show a central peak and ring-like shoulders. In Peakorino, the data points were fitted with three Lorentzian functions, using one Lorentzian for the central peak and two Lorentzians for the ring-like broadening (Fig 5.14). The parameters of two Lorentzians describing the ring-like broadening (FWHM and intensity) were coupled. The full width at half maximum (FWHM) of the central spike was fixed to $0.7\,\%\,BZ$ since the fitting profile variations were too small (almost a constant).
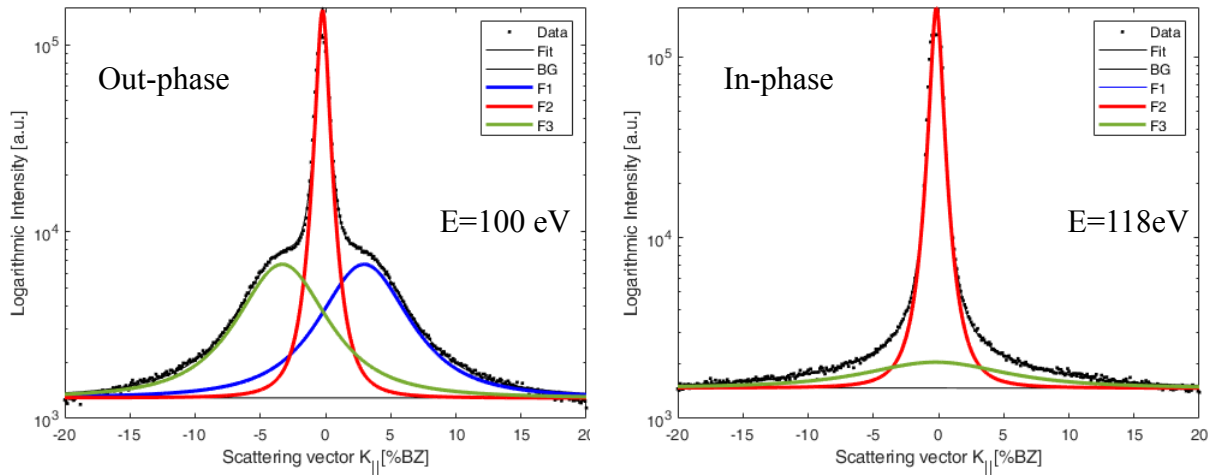
Fig 5.14: Splitting of (00) reflex showing a ring-like broadening and a peak. The plot shows the data points fitted with three Lorentzian functions

(Fig 5.15) shows the full width at half maximum (FWHM) of one of the Lorentzians of the ring-like shoulder against the square root of energy. The oscillatory behaviour in the plot with maxima and minima at in-phase and out-of phase conditions is observed and the step height (d) could be concluded. The step height of STO was found with the analysis of scattering phases according to (Eqn. 2.28). As a result, the step height (d) of STO was calculated to be (3.93 ± 0.03) Å being in accordance with the literature value of STO is 3.9051 Å within the experimental uncertainties.
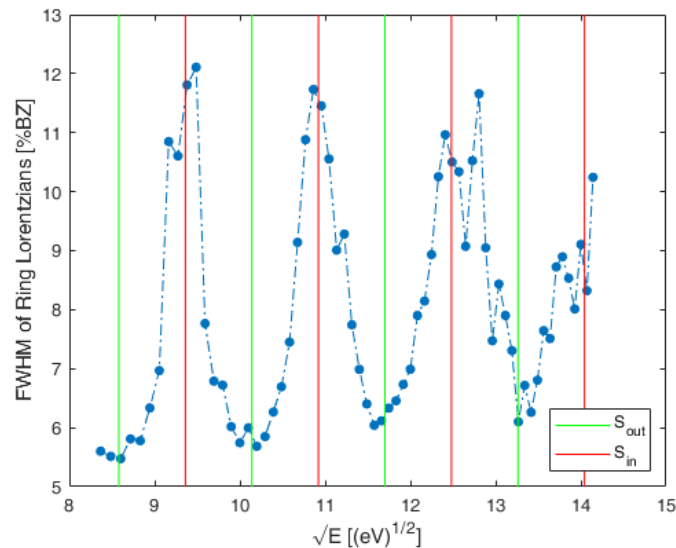

Fig 5.15: FWHM of ring Lorentzians with in-phase and out-of-phase conditions

The terrace width cannot be calculated only from the FWHM of the ring Lorentzians. Hence, the diameter of the ring is taken into account. As mentioned in (Chapter 2.3.4), the standard deviation

$\sigma/\langle\Gamma\rangle$ can be obtained from the ratio of spot splitting and FWHM. At out-of-phase condition, the ring diameter is $6\,\%\,BZ$ (Fig 5.16) and FWHM is $6\,\%\,BZ$ (Fig 5.15), thus the ratio of $2K_o/FWHM$ is 1, which is the same value obtained from the analysis of $400°C$ (Chapter 5.3). Hence, the results from [31] applies here too. It is seen that when the ratio of spot splitting and FWHM is 1 then $\sigma/\langle\Gamma\rangle$ is 0.72 (Fig 5.9), thus supporting the experimental result.

From (Fig 5.15), it is seen that the out-of-phase condition is at minima with a FWHM of (5.9 ± 0.1) $\%\,BZ$. With respect to (Eqn. 2.29) and with FWHM, the average terrace width $\langle\Gamma\rangle$ from the broad shoulder is deduced to be (31.7 ± 0.1) Å. The (Fig 5.15) also shows that the in-phase condition is at the maxima with a FWHM of $(11.6 \pm 0.2)\,\%\,BZ$. In addition, the ring radius vanishes at in-phase (Fig 5.16), meaning the domain size can be calculated from the "normal" formula (Eqn. 2.29) having only one broad Lorentzian. Thus the average domain size (D) is calculated to be (16.4 ± 0.2) Å.
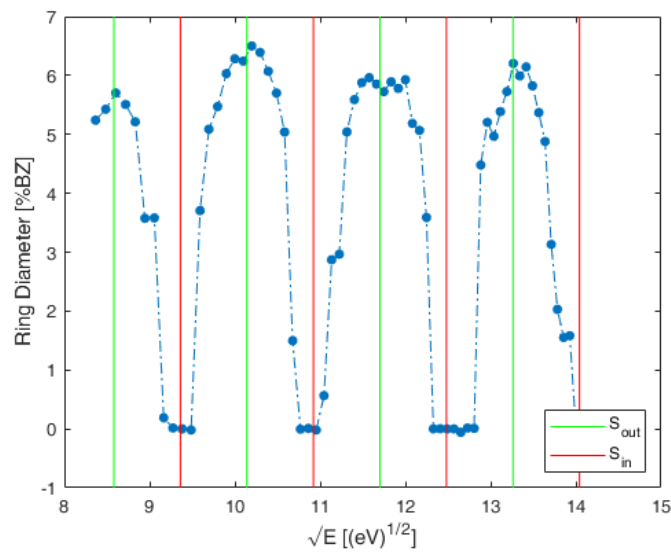

Fig 5.16: Ring diameter with in-phase and out-of-phase conditions

As stated in (Chapter 5.4), the central peak's full width at half maximum (FWHM) of the central spike was fixed to $0.7\,\%\,BZ$ and the transfer width was calculated to be $(55.8 \pm 0.1)\,nm$.

(Fig 5.17) shows lattice factor G(S) against square root energy. Where the lattice factor G(S) was calculated from the (Eqn. 2.23). The periodic oscillations of the lattice factor with scattering phase is a result of the presence of steps. In accordance with the former analysis of FWHM, the step height (d) of STO is calculated to be (3.93 ± 0.03) Å from (Eqn. 2.28) being in accordance with the literature value of STO 3.905 Å with experimental uncertainties.
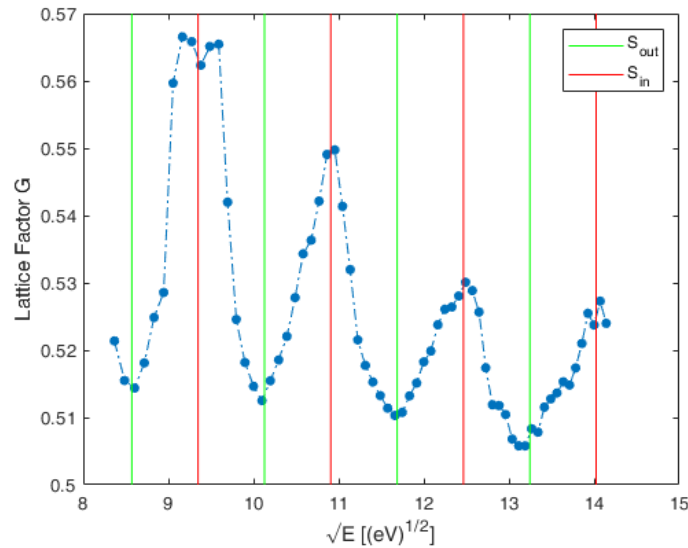

Fig 5.17: Lattice factor G with in-phase and out-of-phase conditions

(Fig 5.17) shows the maxima and minima are at in-phase and out-of-phase conditions respectively. The $G(S)$ value reaches a maximum of (0.57 ± 0.01) and does not go to 0 which means that the shoulders don't completely disappear at the in-phase condition and peaks don't vanish at the out-of-phase condition. This could be because of defects such as inhomogeneities and atomic steps, respectively. In addition, the decline in oscillation with respect to energy can be attributed to small variation of lattice or atomic distance.

The (Fig 5.18) shows peaks of $G(S)$, fitted with gaussian functions. The values of FWHM of the respective peaks were applied in (Eqn. 2.27) and the surface roughness (Δ) is found to be (2.43 ± 0.02) Å. The variation of surface roughness with respect to change in temperature is discussed in (Chapter 5.6).
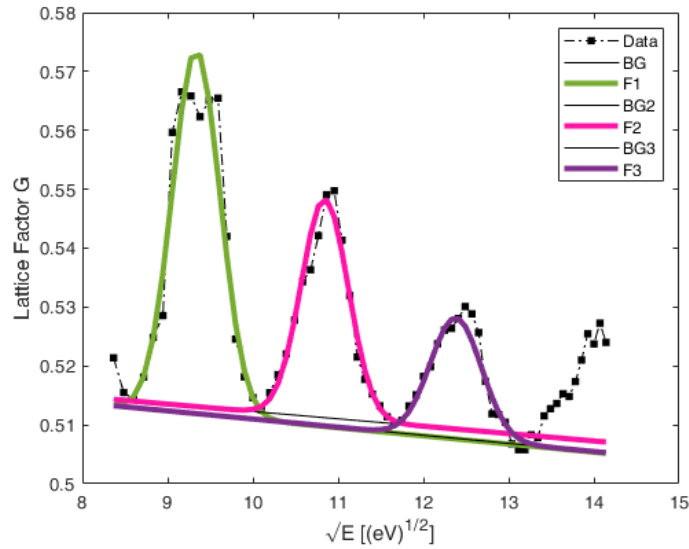
Fig 5.18: The three in-phase conditions of lattice factor G approximated with a Gaussian function to estimate the surface roughness from their FWHM

5.5. Results of sample treated at 800°C

In Peakorino, the data points of sample that was treated at a temperature of 800°C were fitted with two Lorentzian functions (Fig 5.19). It comprises of a broad shoulder and a central peak. In addition to this, mosaic diffraction peaks were seen at few energies. Mosaics were seen at an energy range of 70 eV to 140 eV. Mosaic peaks could not be seen at higher energies as they ran out of the range.
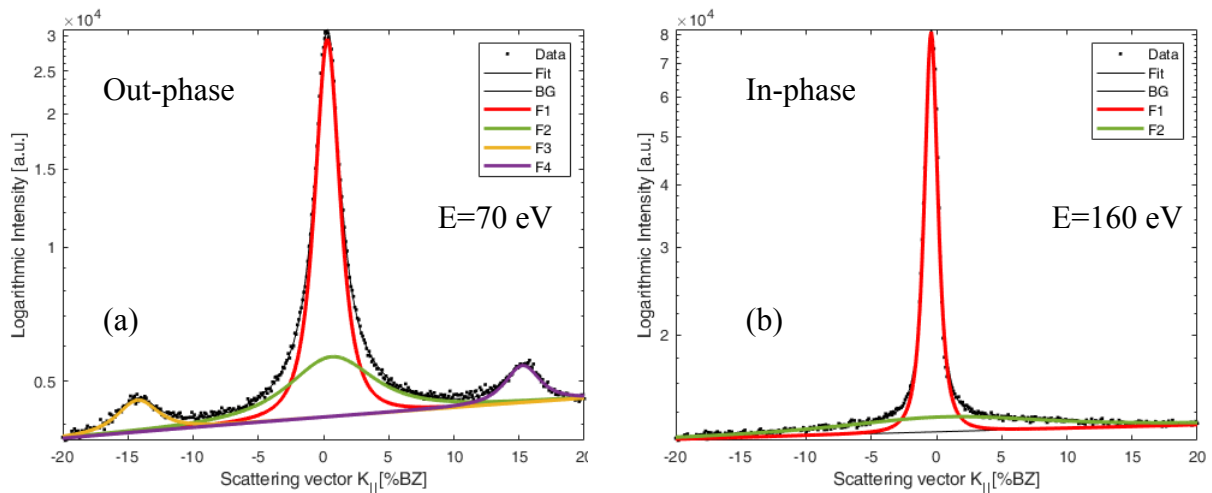

Fig 5.19: Splitting of (00) reflex into a broad shoulder and a central peak. The plot shows the data points fitted with two Lorentzian functions. (a) Mosaic diffraction peaks were coupled and fitted with Lorentzian functions. (b) Mosaic peaks ran out of the measuring range hence, could not be seen

46

(Fig 5.20) shows the full width at half maximum (FWHM) of broad shoulder against square root of energy. The oscillatory behaviour in the plot with maxima and minima at in-phase and out-of-phase conditions is observed. The step height of STO was found with the analysis of scattering phases according to (Eqn. 2.28). As a result, the step height of STO was calculated to be (3.93 ± 0.03) Å. The literature value of STO is 3.905 Å. Thus, within experimental uncertainties, the value from experiment agrees well with the value reported in literature.
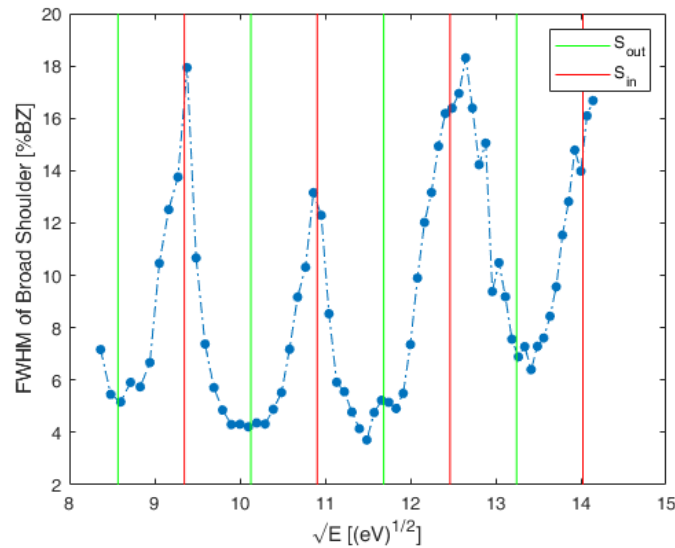

Fig 5.20: FWHM of broad shoulder with in-phase and out-of-phase conditions

From (Fig 5.20) it is seen that the minima with a FWHM of (4.8 ± 0.5) $\%\,BZ$ are at out-of-phase. With respect to (Eqn. 2.29) and with FWHM, the average terrace width $\langle \Gamma \rangle$ from the broad shoulder is deduced to be (39.9 ± 0.5) Å. The (Fig 5.20) also shows that the maxima with a FWHM of $(16.2 \pm 2)\,\%\,BZ$ are at in-phase conditions. Thus the average domain size (D) is calculated to be (11.8 ± 2) Å.

(Fig 5.21) shows the full width at half maximum (FWHM) of the central peak against square root energy. The oscillatory behaviour with maxima and minima at out-of-phase and in-phase conditions is observed in the plot and the step height (d) could be concluded.
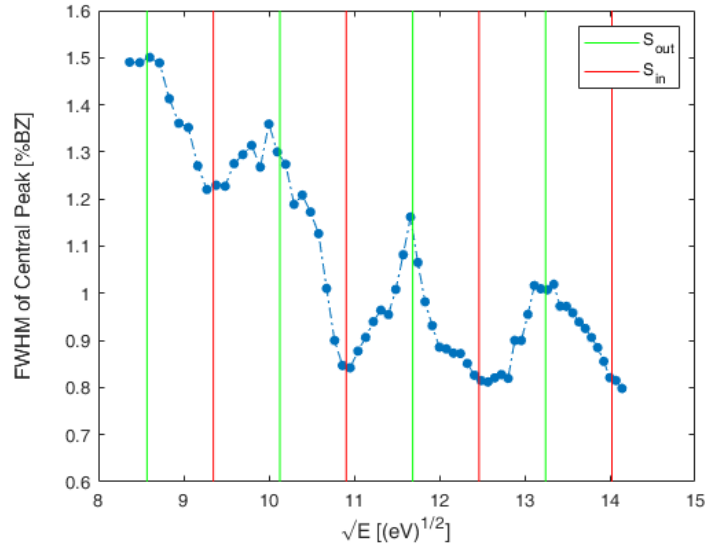
Fig 5.21: FWHM of central peak with in-phase and out-of-phase conditions

The step height of STO was found with the analysis of scattering phases according to (Eqn. 2.28). As a result, the step height (d) of STO was calculated to be (3.93 ± 0.03) Å being in accordance with the literature value of STO, 3.905 Å with experimental uncertainties. From (Fig 5.21) it is seen that the in-phase condition is at minima with a FWHM of $(1.0 \pm 0.1)\,\%\,BZ$. With respect to (Eqn. 2.39), the transfer width is calculated to be $(39.1 \pm 0.2)\,nm$.
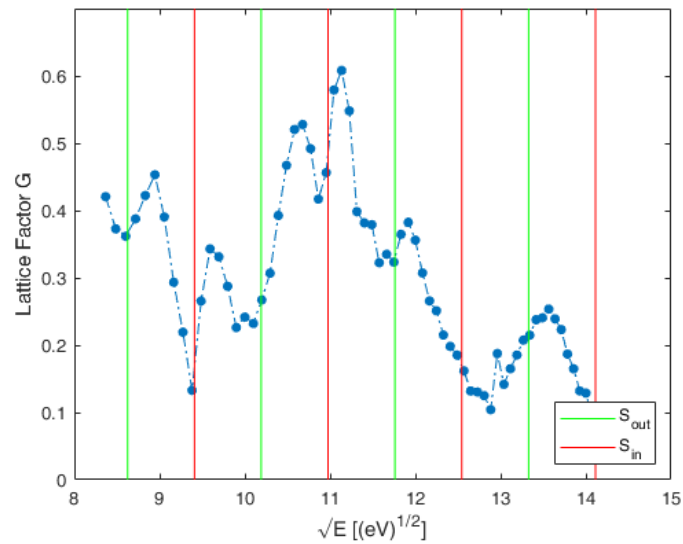

Fig 5.22: Lattice factor G with in-phase and out-of-phase conditions which does not match the earlier experimental conditions in terms of minima and maxima due to the possibility of lattice distortion

48

(Fig. 5.22) shows lattice factor G(S) against square root energy. However, the plot looks strange as the in-phase and out-of-phase conditions are different from that of the earlier discussed temperature ranges. This is maybe due to the presence of too many defects. It might be the case of a lattice distortion. Hence, further analysis could not be made.

As mentioned in (Chapter 2.3.5), the evaluation of the mosaic angle can be calculated from the linear increase of the position of the mosaic diffraction peak with increasing vertical scattering vector being proportional to $\sqrt{E}$. In (Fig 5.23), the slope is $2.2\,\%\,BZ/(eV)^{1/2}$. Thus from (Eqn. 2.37) the mosaic angle is deduced to be 2.0°.
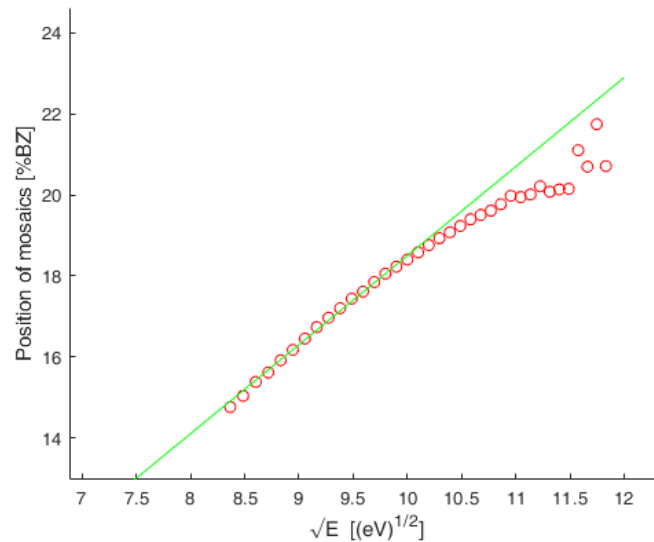
Fig 5.23: Shows the inclined slope (green line) drawn from the position of mosaics (red circles) from which the mosaic spread was estimated

In (Fig 5.23), it is seen that the data points are not linear over the energy range of 10 $(eV)^{1/2}$. This is due to the mosaic reflexes that move away from the (00) and reaches the measurement limit. As a result, the position cannot be fitted properly and hence, there is a huge error in this area.

5.6. Trend of half-width, surface roughness and terrace width at varied temperatures

(Fig 5.24) shows the full width at half maximum of the diffuse broadening at out-of-phase condition at an energy of 100 eV against their preparation temperature. As mentioned in (Chapter 2.3.4), the FWHM of shoulder is an indicator for terrace width size. Here, FWHM of diffuse shoulder decreases with increase in temperature indicating the increase in terrace size when treated at higher temperatures.
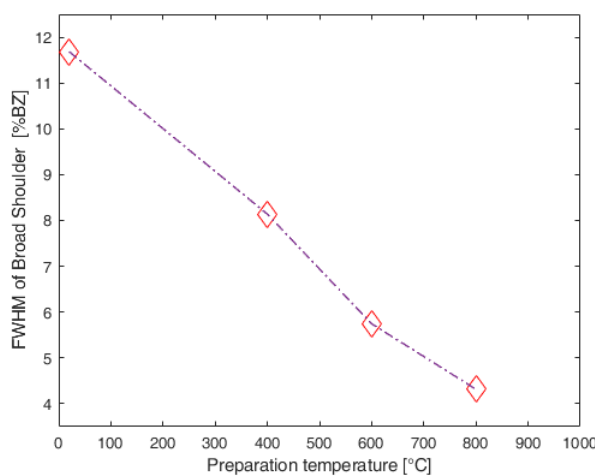

Fig 5.24: Graph showing the decrease in FWHM of diffuse broadening that indicates the increase in average terrace size with rise in temperature. Illustration of 100 eV energy. The dotted line is just a guide to the eye

(Fig 5.25 (a)) shows the full width at half maximum of the diffuse broadening at in-phase condition at an energy of 118 eV against their preparation temperature. Here, FWHM of broad shoulder decreases at untreated, $400°C$ and $600°C$ followed by an increase in FWHM at $800°C$. (Fig. 5.25 (b)) shows the full width at half maximum of the central peak at in-phase condition at an energy of 88 eV against their preparation temperature. Here, FWHM of central peak increases at untreated and $400°C$ followed by a decrease in FWHM at $600°C$. Then, at $800°C$ there is an increase in FWHM of the central peak. Considering the measuring error there is an increase of FWHM with temperature.
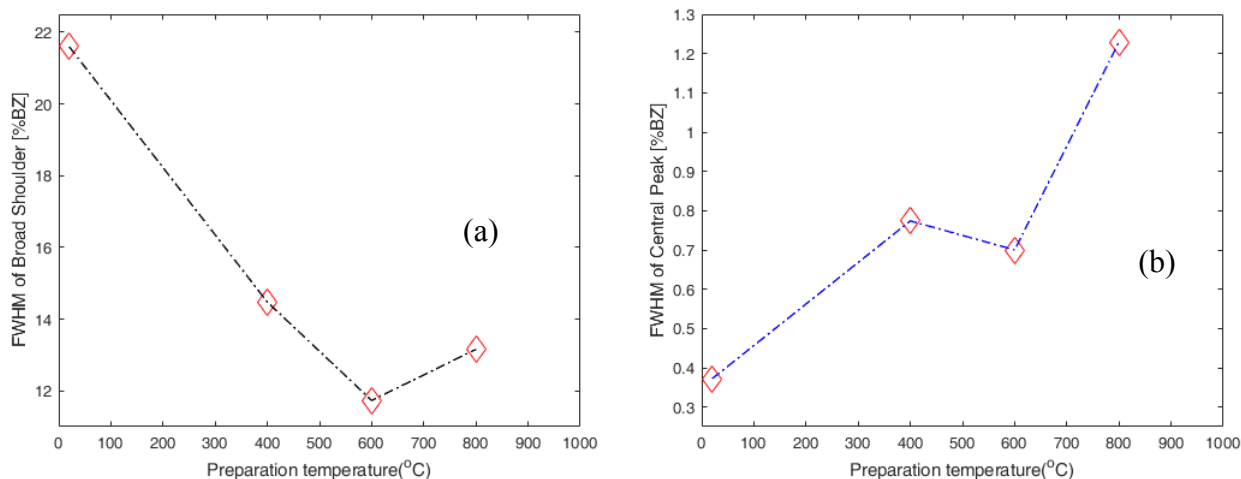
Fig 5.25: (a) Graph showing the FWHM of broad shoulder at in-phase condition at an energy of 118 eV. (b) Graph showing the FWHM of central peak at in-phase condition at an energy of 88 eV. The dotted line is just a guide to the eye

In (Fig 5.26) the surface roughness (Δ) calculated from G(S) of different samples is plotted against their preparation temperature and it is evident that the roughness of surface increases with temperature. Thus, the surface of STO becomes rougher in vertical direction with the rise in preparation temperature.
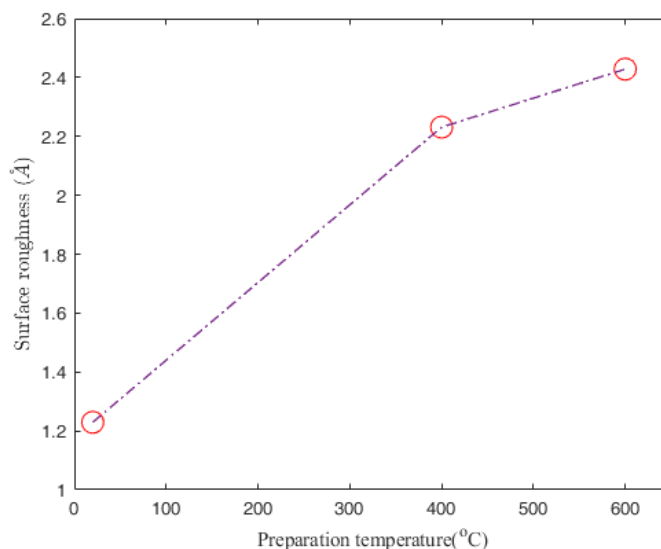

Fig 5.26: Illustration of the increase in surface rms-roughness (Δ) with increase in preparation temperature. The dotted line is just a guide to the eye

In (Fig 5.27), the average terrace width of different samples are plotted against their preparation temperature in order to show the increase in width of terraces with respect to treatment at higher

51

temperatures. (Fig 5.27) shows that at out-of-phase conditions, the terrace width increases with increase in temperature. Thus, the surface roughness decreases in lateral direction
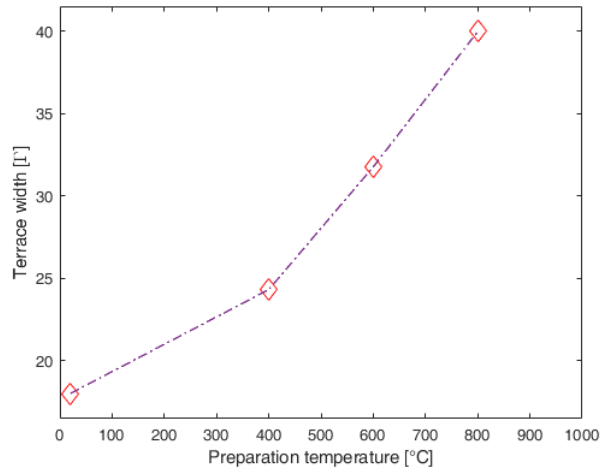
Fig 5.27: Graph shows the surge in terrace width with increase in preparation temperature at out-of-phase conditions. The dotted line is just a guide to the eye

In (Fig 5.28), the average domain size (D) at in-phase conditions of different samples are plotted against their preparation temperature. The domain size of samples increase at untreated, $400°C$ and $600°C$. Then, the domain size decreases when the sample is treated at $800°C$.
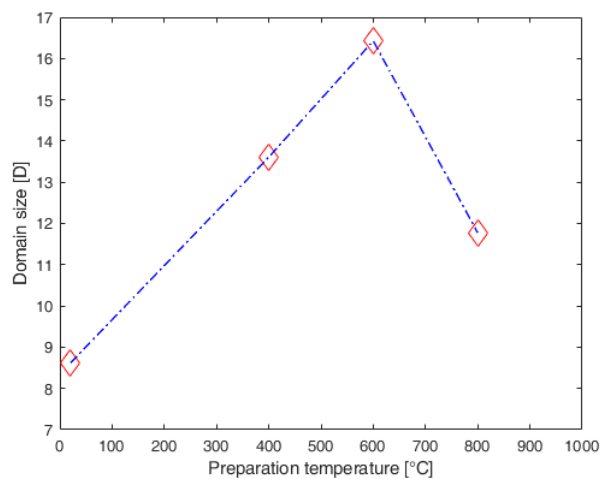
Fig 5.28: Shows an increase in domain size until $600°C$ and then there is a decrease in domain size as the temperature is increased to $800°C$ at in-phase conditions. The dotted line is just a guide to the eye

6 Summary and outlook

In this thesis, the different preparation conditions of STO (001) surfaces were investigated. The sample was treated at various temperatures in the presence of oxygen with a pressure $1 \times 10^{-4} mbar$ for 1 hour and the surface morphology like steps, terrace widths and roughness of surface were studied. Morphology of the surface was examined by SPA-LEED [28]. The results obtained confirm the presence of defects (atomic steps, inhomogeneities etc.,) on the surface of the sample.

Initially, the sample was prepared at room temperature without any treatment and was analysed. Further experiments were carried out by treating the sample at $400°C$, $600°C$ and $800°C$ in the presence of O_2. It is seen from the experiment that for the untreated sample and sample treated at $800°C$, there is only one shoulder whereas for the samples treated at $400°C$ and $600°C$, there are ring-like shoulders. The half-width and position of shoulders give the average terrace width and standard deviation of the terrace width distribution as mentioned in [31]. It is seen from the experiment that the half-width decreases with increase in temperature which means that the terrace width is increasing. The study also shows that the rms-roughness of surfaces become rougher with the increase in annealing temperature. Thus, the vertical roughness increases with increasing preparation temperature while the lateral roughness decreases. However, from the analysis of sample's surface prepared at $800°C$, it is seen that the surface gets distorted at high temperatures. Hence, surfaces should not be treated too harshly as it promotes to many defects. At $800°C$, appearance of mosaics on the substrate's surface could be seen which is not ideal for film growths on STO surfaces as it may result in various other defects like facets on the film surface.

For further studies, preparation of samples can be carried out with no or less oxygen by leaving the sample only in UHV conditions and by treating them at different temperatures. In addition, more oxygen could also be helpful as well as the use of oxygen plasma. This could be an alternative so as to avoid lattice distortion due to high temperatures.

7 Bibliography

1.   Wolf, S., et al., Spintronics: a spin-based electronics vision for the future. science, 2001. **294**(5546): p. 1488-1495.

2.   Binasch, G., et al., Enhanced magnetoresistance in layered magnetic structures with antiferromagnetic interlayer exchange. Physical review B, 1989. **39**(7): p. 4828.

3.   Gallagher, W.J. and S.S. Parkin, Development of the magnetic tunnel junction MRAM at IBM: From first junctions to a 16-Mb MRAM demonstrator chip. IBM Journal of Research and Development, 2006. **50**(1): p. 5-23.

4.   Hirohata, A., et al., Review on spintronics: Principles and device applications. Journal of Magnetism and Magnetic Materials, 2020. **509**: p. 166711.

5.   Carpentieri, M. and G. Finocchio, Applications of Magnetic Materials and Spintronics in Smart Systems. 2022.

6.   Parkinson, G.S., et al., Tailoring the interface properties of magnetite for spintronics. 2012: INTECH Open Access Publisher.

7.   Bliem, R., et al., Subsurface cation vacancy stabilization of the magnetite (001) surface. Science, 2014. **346**(6214): p. 1215-1218.

8.   Takahashi, K., et al., Inverse tunnel magnetoresistance in all-perovskite junctions of La 0.7 Sr 0.3 MnO 3/SrTiO 3/SrRuO 3. Physical Review B, 2003. **67**(9): p. 094413.

9.   Shende, R.V., et al., Strontium zirconate and strontium titanate ceramics for high−voltage applications: synthesis, processing, and dielectric properties. Journal of the American Ceramic Society, 2001. **84**(7): p. 1648-1650.

10.   McColm, T. and J. Irvine, B site doped strontium titanate as a potential SOFC substrate. Ionics, 2001. **7**(1): p. 116-121.

11.   Singh, R., et al., Thermal tunability in terahertz metamaterials fabricated on strontium titanate single-crystal substrates. Optics letters, 2011. **36**(7): p. 1230-1232.

12. Kuschel, O., From initial growth of ultrathin Fe3O4 films up to NiFe2O4 formation through interdiffusion of Fe3O4/NiO bilayers on Nb: SrTiO3 (001). 2020, Universität Osnabrück.

13. Kittel, C. and P. McEuen, Introduction to solid state physics. 2018: John Wiley & Sons.

14. Bragg, P., *Bragg WL Proc. R.* Soc. London. Ser. A, Contain. Pap. a Math. Phys. Character, 1913. **17**: p. 428.

15. Friedrich, W., P. Knipping, and M. Laue, Interferenzerscheinungen bei roentgenstrahlen. Annalen der Physik, 1913. **346**(10): p. 971-988.

16. Wood, E.A., Vocabulary of surface crystallography. Journal of applied physics, 1964. **35**(4): p. 1306-1312.

17. Oura, K., et al., *Surface science: an introduction*. 2013: Springer Science & Business Media.

18. Nordmann, T., Epitaxy of ultrathin nickel ferrite films on MgO(001) and SrTiO3(001), in Physics. 2016, University of Osnabrück. p. 77.

19. Davisson, C. and L.H. Germer, The scattering of electrons by a single crystal of nickel. Nature, 1927. **119**(2998): p. 558-560.

20. Thien, J., From Magnetite to Cobalt Ferrite Thin Films: New Perspectives for the Growth of Thin Ferrite Films for their Application in Spintronics, in Physics. 2022, University of Osnabrück. p. 141.

21. Berlekamp, S., Electronic, optical and transport properties of ultrathin cobalt ferrite films on MgO(001), in Physics. 2021, University of Osnabrück. p. 72.

22. Bahlmann, J., Advances in Structural LEED Analyses of Silicon Surfaces, in Physics. 2022, University of Osnabrück. p. 109.

23. Schuckmann, O., Plasmamodifizierung von Praseodym- und Ceroxidschichten, in Physics. University of Osnabrück.

24. Henzler, M., Measurement of surface defects by low-energy electron diffraction. Applied Physics A, 1984. **34**(4): p. 205-214.

25. Henzler, M., Defects at semiconductor surfaces. Surface Science, 1985. **152-153**: p. 963-976.

26. VanHove, M.A., W.H. Weinberg, and C.-M. Chan, Low-energy electron diffraction: experiment, theory and surface structure determination. Vol. 6. 2012: Springer Science & Business Media.

27. Sprenger, K., SPA-LEED examinations of Gd and Tb silicide monolayers on Si(001), in Physics. 2021, University of Osnabrück. p. 99.

28. Horn-von Hoegen, M., Growth of semiconductor layers studied by spot profile analysing low energy electron diffraction.

29. Park, R.L. and J. Houston, The effect of registry degeneracy on LEED beam profiles. Surface Science, 1969. **18**(2): p. 213-227.

30. Houston, J. and R.L. Park, Low-energy electron diffraction from imperfect structures. Surface Science, 1970. **21**(2): p. 209-223.

31. Wollschläger, J., Simple analysis of spot splitting due to diffraction at surfaces with atomic steps. Surface science, 1997. **383**(1): p. 103-122.

32. Wollschläger, J., J. Falta, and M. Henzler, Electron diffraction at stepped homogeneous and inhomogeneous surfaces. Applied Physics A, 1990. **50**(1): p. 57-68.

33. Lent, C. and P. Cohen, Diffraction from stepped surfaces: I. Reversible surfaces. Surface science, 1984. **139**(1): p. 121-154.

34. Alexander, A., SPA-LEED-Untersuchungen zum Wachstum von auf (001), in Physics. 2019, University of Osnabrück.

35. J.Wollschläger, SPA-LEED-Untersuchungen an der Grenzfläche Silizi- um/Siliziumdioxid, in Physics. 1986, Universität Hannover.

36. Wollschläger, J., Diffraction from surfaces with randomly distributed structural defects. Surface science, 1995. **328**(3): p. 325-336.

37. Henzler, M., *LEED studies of surface imperfections.* Applications of Surface Science, 1982. **11**: p. 450-469.

38. Nedkov, I. and M. Ausloos, Nano-Crystalline and Thin Film Magnetic Oxides: Proceedings of the NATO Advanced Research Workshop on Ferrimagnetic Nano-Crystalline and Thin

Film Magnetooptical and Microwave Materials Sozopol, Bulgaria Sept. 27–Oct. 3, 1998. Vol. 72. 1999: Springer Science & Business Media.

39.   Cardona, M., Optical Properties and Band Structure of SrTi O 3 and BaTi O 3. Physical Review, 1965. **140**(2A): p. A651.

40.   Schafranek, R., et al., The SrTiO3/BiFeO3 (001) interface: commutativity of energy band discontinuities. New Journal of Physics, 2013. **15**(5): p. 053014.

41.   Coey, J., M. Venkatesan, and P. Stamenov, *Surface magnetism of strontium titanate.* Journal of Physics: Condensed Matter, 2016. **28**(48): p. 485001.

42.   Tomio, T., et al., Control of electrical conductivity in laser deposited SrTiO3 thin films with Nb doping. Journal of Applied Physics, 1994. **76**(10): p. 5886-5890.

43.   Bruns, D., Structure and morphology of ultrathin iron and iron oxide films on Ag (001). 2012.

44.   Gevers, S., SPA-LEED-Untersuchungen von Praseodymoxidschichten auf Si (111)-Substraten, Universität Osnabrück. 2007, Diplomarbeit.

Erklärung zur selbstständigen Abfassung der Masterarbeit

59

Name: Nandhini Ravindran

Geburtsdatum: 20.10.1997

Matrikelnummer: 988301

Titel der Masterarbeit: *Preparation of $SrTiO_3$ (001) Surfaces Studied by SPA-LEED*

Ich versichere, dass ich die eingereichte Masterarbeit selbstständig und ohne unerlaubte Hilfe verfasst habe. Anderer als der von mir angegebenen Hilfsmittel und Schriften habe ich mich nicht bedient. Alle wörtlich oder sinngemäß den Schriften anderer Autoren entnommenen Stellen habe ich kenntlich gemacht.

Osnabrück, 23.02.2023

_____   _____
Ort, Datum   Unterschrift

Acknowledgement

I profusely thank Prof. Dr. Joachim Wollschläger for giving me the opportunity to work in his group "Dünne Schichten und Grenzflächen". I thank him for his guidance throughout my Master thesis and for all the fruitful discussions from which I learnt a lot. Visit to DESY and SPA-LEED workshop was a great academic experience to me. Thanks in abundant measure are due to him for being kind, humble and for being a great mentor. I really value the time I spent around with him during my academic stay in Germany.

My sincere thanks to Dr. Karsten Küpper for agreeing to be my second examiner. I thank him for checking the progress of my thesis. My thanks are due to him for the friendly gesture.

I would like to thank Andreas Alexander for supervising and helping me in experiments and for clearing my umpteen number of doubts with regard to my thesis. I thank him for the kind support.

I would like to thank Alexander Weißbach for being supportive from Day 1 of my thesis and checking on my wellness. His radiant greetings lifted my spirits and comforted whenever I was running into difficulties.

I thank Eugenia Miller for her love and care. She helped me with official University documents. I thank Tobias Pollenske for being a great friend, for his warm smile and to whom I ran for help any time of the day.

I extend my thanks to all the members of AG Wollschläger for their support and sharing their experience in academics.

My special thanks go to my dearest parents (*Appa* and *Amma*) who live 7000 km away from me but still made me feel that they were there at all points of my academic journey. Their faith in me, unwavering encouragement, great moral support and abundant love has helped me to complete my Master's degree successfully. I thank my dear *swami thatha* for his kind blessings and constant motivation. I thank my dear *ammuma* for her blessings and all my dear friends for their love and support.